High-Order Shock-Fitting Method for Hypersonic Flow with Graphite Ablation and Boundary Layer Stability

Clifton H. Mortensen* and Xiaolin Zhong†
University of California, Los Angeles, California, 90095, USA

A high-order shock-fitting method with thermochemcial nonequilibrium and finite rate boundary conditions for graphite ablation is presented. The method is suitable for direct numerical simulation of boundary layer stability with graphite ablation. Validation with three computational data sets and one set of experimental data is shown. Stability results of the method for a 7° half angle blunt cone at Mach 15.99 are compared with ideal gas computations that set their wall temperature and wall blowing from the real gas simulation. Weak planar fast acoustic waves are used to perturb the steady base flow. In the nose region wall normal velocity fluctuations increase three orders of magnitude and then decrease rapidly as the wall mass flux decreases on the cone surface. In the nose region perturbation amplitudes of vibration temperature are two orders of magnitude larger than perturbation ampitudes of translation-rotation temperature.

Nomenclature

C	Mass fraction
$c_{v,s}$	Species translation-rotation heat capacity at constant volume J/kgK
D	Species diffusion coefficient m^2/s
e	Specific total energy J/kg
$e_{v,s}$	Species specific vibration energy J/kg
e_v	Specific vibration energy J/kg
h_o	Stagnation enthalpy J/kg
h_s^o	Species heat of formation J/kg
M_s	Species molecular weight kg/mol
$\dot{m}'$	Mass flux per area $kg/m^2 \cdot s$
n	Surface normal
nms	Number of molecular species
ns	Number of species
$Q_{T-V,s}$	Species vibration energy transfer rate J/s
R	Universal gas constant, 8.3143 $J/mol \cdot K$
r	Sphere radius
s	Surface streamline
v_w	Wall normal velocity m/s

Subscripts

∞	Freestream
n	Normal component
s	Species
t	Tangential component
w	Wall

Symbols

δ_{ij}	Kronecker delta
ω_s	Rate of species production $kg/m^3 \cdot s$
ρ	Density kg/m^3

I. Introduction

Ablating thermal protection systems are commonly used to protect hypersonic vehicles from the harsh aerothermal environment they operate in.[1] Examples include ablative heat shields for hypersonic reentry vehicles, throat liners inside rocket engines, and nose cones or fins for thermal protection of hypersonic missiles. The design of these thermal protection systems is of major concern to the vehicle designer who must ensure the structural integrity of the vehicle throughout its flight envelope. The design of thermal protection systems is an iterative process requiring the evaluation of many configurations in order to determine the optimal. Experimental testing of the various designs can be done in the laboratory or by flight tests. However

*Graduate Student, Mechanical and Aerospace Engineering, cmort22@gmail.com, AIAA Student Member.
†Professor, Mechanical and Aerospace Engineering, xiaolin@seas.ucla.edu, AIAA Associate Fellow.

the laboratory simulation of all required hypersonic flow conditions may not be possible. Likewise, flight tests are expensive and time consuming. Thus, numerical simulations today are assuming an increasingly important role as a cost-effective complement to laboratory and flight test research.

Practical methods for ablation prediction employ various levels of simplification, ranging from empirical engineering correlation and approximate semi-empirical integral methods, to very detailed full Navier-Stokes simulation methods that model the nonequilibrium chemically reacting fluid dynamics coupled to in-depth heat conduction material models.[2–7] Surface chemistry models are commonly used in full Navier-Stokes simulations to more accurately model surface species concentrations and mass blowing rates. Some common surface chemistry models are that of Zhluktov and Abe[8] and Park.[9,10]

An added difficulty to ablation prediction is prediction of boundary layer transtion. Boundary layer transition has a strong effect on the estimation of heating rates for earth reentry vehicles. A turbulent boundary layer has a much higher heating rate than a corresponding laminar boundary layer. In turn the heating rates impact the design of a space vehicle's thermal protection system which has a strong impact on the overall weight and cost of the vehicle. Laminar-turbulent transition in hypersonic boundary layers is a complex phenomena involving multiple factors such as freestram disturbances, receptivity, surface roughness, and multiple transition paths. When ablation is accounted for there are added difficulties such as shape change, ablation induced roughness, gas influx at the surface, thermochemical nonequilibrium, introduction of new chemical species and the reactions of those species with the freestream gas. Numerical modeling of transition phenomena plays an important role in studying hypersonic boundary layer transition as it can be extremely difficult to replicate exact flight conditions in wind tunnels.

Most research on stability of hypersonic boundary layers has been performed with a perfect gas model and few researchers have studied thermochemical nonequilibirium effects. Significant research on the linear stability of boundary layers has been performed by Mack.[11] Mack found that the major instability waves for hypersonic boundary layers with a perfect gas assumption are the first and second modes. Following researchers have implemented numerical codes using linear stability theory to compute the most unstable frequencies for a variety of flow conditions and gas models. Malik[12] implemented multiple numerical methods for linear stability of perfect gas boundary layer flows. Stuckert and Reed,[13] Hudson et al.,[14] and Johnson et al.[15] studied laminar-turbulent transition in nonequilibrium chemically reacting hypersonic boundary layers using linear stability theory. It was found that dissociation of air species is destabilizing to the second mode and stabilizing to the first mode. Ma and Zhong[16] studied the receptivity of free stream disturbances of a Mach 10 nonequilibrium oxygen flow over a flat plate. They found that in a Mach 10 oxygen flow there is a significant real gas destabilizing effect on the second-mode waves. However they did not consider thermal nonequilibrium or any gas/surface interaction. Prakash et al.[17] studied receptivity of freestream disturbances with a thermochemical nonequilibrium shock-fitting method. Parsons et al.[18] studied the receptivity effects of thermochemical nonequilibrium on blunt cones. They found that freestream acoustic waves had higher pressure perturbation amplitudes for a flow with thermochemical nonequilibrium than a perfect gas. Also they found that the maximum perturbation amplitude moved nearer to the blunt nose.

Currently there has been a limited amount of numerical research on how ablation and surface chemistry models effect hypersonic boundary layer transition. Johnson et al.[19] used linear stability analysis to analyze non-reacting and reacting hypersonic boundary layer stability with blowing and suction. Ghaffari et al.[20] performed a linear stability analysis of a hypersonic perfect gas flat plate boundary layer with wall blowing and found that as blowing increases the maximum amplification rate of the disturbance instability grows and moves to lower frequencies. Li et al.[21] studied boundary layer instability mechanisms for hypersonic perfect gas flows over slender cones and blunt capsules at zero angle of attack and an angle of attack of 16°. They found that for the slender cone out-gassing is moderately stabilizing to the second mode and for the blunt capsule out-gassing is destabilizing to the first mode.

The goal of this paper is twofold: 1) to validate a shock-fitting thermochemical nonequilibrium eleven species gas code with gas/surface interactions relating to graphite ablation and 2) to study the effect of graphite ablation and thermochemical nonequilibrium on hypersonic boundary layer stability. An eleven species gas model is used to model chemical nonequilibrium. It contains a standard five species air model, N_2, O_2, NO, N, O, without ionization. The remaining species, $C_3, CO_2, C_2, CO, CN, C$, are obtained from sublimation, oxidation and reactions of ablation products with five species air. A two-temperature model is used to simulate thermal nonequilibrium. Only graphite ablation is considered without the effects of charring, pyrolysis, surface recession and ablation induced roughness. The surface reactions considered contain oxidation, recombination of atomic oxygen and sublimation. A surface mass balance is used to set

species mass fractions at the surface and temperature profiles within the ablator are not computed. The authors would like to point out that much of the work performed by Keenan[2] and Keenan and Candler[22,23] has served as a basis for the gas phase models as well as the surface chemistry model used here.

The paper will start with an overview of the governing equations and the gas phase models followed by an overview of the surface chemistry model as well as the required boundary conditions. After which the shock-fitting scheme with the implemented models will be validated with cases computed by Keenan.[2] Then the code will be compared to a graphite ablation case computed by Chen and Milos[4] with corresponding experimental data. After code validation, one case is run of a 7° half angle blunt cone at Mach 15.99 to study hypersonic boundary layer transition with thermochemical nonequilibrium and graphite ablation.

II. Governing Equations and Gas Phase Models

A high-order shock-fitting method developed by Zhong[24] is used to compute the flowfield between the shock and the body. The inviscid terms are discretized using a 5^{th} order upwinded difference and the viscous terms are discretized using a 6^{th} order central scheme. Conditions behind the shock are calculated from Rankine-Hugoniot relations. Low storage 3^{rd} order Runge-Kutta or explicit Euler is used to advance the solution in time. The governing equations for thermochemical nonequilibrium are formulated for a two-temperature model with the rotational energy mode assumed to be fully excited and eleven non-ionizing species with finite rate chemistry. Two temperatures are used to represent translation-rotation energy and vibration energy. The eleven species model $(N_2, O_2, NO, C_3, CO_2, C_2, CO, CN, N, O, C)$ is used to simulate air, surface reactions, and reactions of air with ablation products. The conservative three-dimensional Navier-Stokes equations consist of eleven species mass conservation equations, three momentum conservation equations, the vibration energy conservation equation and the total energy conservation equation. Written in vector form the equations are

$$\frac{\partial U}{\partial t} + \frac{\partial F_j}{\partial x_j} + \frac{\partial G_j}{\partial x_j} = W \tag{1}$$

where U is the state vector of conserved quantities and W is the source terms defined by

$$U = \begin{bmatrix} \rho_1 \\ \vdots \\ \rho_{ns} \\ \rho u_1 \\ \rho u_2 \\ \rho u_3 \\ \rho e \\ \rho e_v \end{bmatrix}, \quad W = \begin{bmatrix} \omega_1 \\ \vdots \\ \omega_{ns} \\ 0 \\ 0 \\ 0 \\ 0 \\ \sum_{s=1}^{nms} \left(Q_{T-V,s} + \omega_s e_{v,s} \right) \end{bmatrix}.$$

F_j and G_j are the inviscid and viscous fluxes respectively and are defined by

$$F_j = \begin{bmatrix} \rho_1 u_j \\ \vdots \\ \rho_{ns} u_j \\ \rho u_1 u_j + p\delta_{1j} \\ \rho u_2 u_j + p\delta_{2j} \\ \rho u_3 u_j + p\delta_{3j} \\ (\rho e + p)\, u_j \\ \rho e_v u_j \end{bmatrix}, \quad G_j = \begin{bmatrix} \rho_1 v_{1j} \\ \vdots \\ \rho_{ns} v_{nsj} \\ \tau_{1j} \\ \tau_{2j} \\ \tau_{3j} \\ -u_i \tau_{ij} - k_T \frac{\partial T}{\partial x_j} - k_V \frac{\partial T_V}{\partial x_j} + \sum_{s=1}^{nms} \rho_s h_s v_{sj} \\ -k_V \frac{\partial T_V}{\partial x_j} + \sum_{s=1}^{nms} \rho_s e_{v,s} v_{sj} \end{bmatrix}$$

where $v_{sj} = u_{sj} - u_j$ is the species diffusion velocity and $\tau_{ij} = \mu\left(\frac{\partial u_i}{\partial x_j} + \frac{\partial u_j}{\partial x_i}\right) - \frac{2}{3}\mu\frac{\partial u_k}{\partial x_k}\delta_{ij}$ is the viscous stress. The total energy per unit volume, ρe, is defined by

$$\rho e = \sum_{s=1}^{ns} \rho_s c_{v,s} T + \rho e_v + \frac{1}{2}\rho u_i u_i + \sum_{s=1}^{ns} \rho_s h_s^o \tag{2}$$

where h_s^o is the heat of formation of species s, $e_{v,s}$ is the species specific vibration energy, and $c_{v,s}$ is the species translation-rotation specific heat at constant volume defined as

$$c_{v,s} = \begin{cases} \frac{5}{2}\frac{R}{M_s}, & s = 1, 2, \ldots, nms \\ \frac{3}{2}\frac{R}{M_s}, & s = nms+1, \ldots, ns. \end{cases} \tag{3}$$

The vibration energy per unit volume, ρe_v, is defined as

$$\rho e_v = \sum_{s=1}^{nms} \rho_s e_{v,s} = \sum_{s=1}^{nms} \rho_s \left(\sum_{m=1}^{nmod} \frac{g_{s,m} R}{M_s} \frac{\theta_{v,s,m}}{\exp\left(\theta_{v,s,m}/T_V\right) - 1} \right) \tag{4}$$

where *nmod* refers to the number of vibrational modes for each polyatomic molecule, $\theta_{v,s,m}$ refers to the characteristic temperature of each vibrational mode, and $g_{s,m}$ is the degeneracy of each vibrational mode. For the diatomic species there is only one vibrational mode and the degeneracy is unity. For C_3 and CO_2 there are three vibrational modes where two modes have a degeneracy of unity and one has a degeneracy of two. The characteristic vibration temperatures and their degeneracies were taken from Park[25] for N_2, O_2 and NO, from Dolton et al.[26] for C_3, and from McBride[27] for CO_2, C_2, CO, and CN.

To model chemical nonequilibrium eight dissociation reactions and sixteen exchange reactions are used. Each reaction is governed by a forward and backward reaction rate determined by Eqs. (5) & (6) respectively. The dissociation reactions are given in Table 1 along with their corresponding forward reaction rate constants in Arrhenius form. The exchange reactions with corresponding forward reaction rate constants are given in Table 2. T_a is the defining temperature for the reaction and is defined as $T_a = \sqrt{TT_V}$ for reactions 1–3 and as $T_a = T$ for all other reactions. When computing the backward reaction rate for all reactions $T_a = T$.

$$k_f = C_f T_a^{\eta} e^{(-\theta_d/T_a)} \tag{5}$$

$$k_b = k_f / K_{eq} \tag{6}$$

The equilibrium coefficent, K_{eq}, is computed in two different ways. For reactions 1–3 and 9–10 a curve fit from Park[25] is employed as in Eq. (7). For the remaining reactions the equilibrium coefficients are computed from Gibbs Free energy and curve fits to the Gibbs Free energy are obtained from McBride et al.[27] as in Eqs. (8) & (9) respectively.

$$K_{eq} = A_0 \exp\left(\frac{A_1}{Z} + A_2 + A_3 \ln(Z) + A_4 Z + A_5 Z^2\right), \quad Z = \frac{10000}{T} \tag{7}$$

$$\frac{G^o}{RT} = a_1(1 - \ln T) - \frac{a_2}{2}T - \frac{a_3}{6}T^2 - \frac{a_4}{12}T^3 - \frac{a_5}{20}T^4 + \frac{a_6}{T} - a_7 \tag{8}$$

$$K_{eq} = \exp\left(-\frac{G^o}{RT}\right)(R_u T)^{-\Delta n} \tag{9}$$

To calculate the source term in the vibration energy equation representing the exchange of energy between the translation-rotation and vibration energies the Landau-Teller expression is used

$$Q_{T-V,s} = \rho_s \frac{e_{v,s}(T) - e_{v,s}(T_V)}{< \tau_s > + \tau_{cs}} \tag{10}$$

where $< \tau_s >$ is the Landau-Teller vibration relaxation time given by Lee[31] defined as

$$< \tau_s > = \frac{\sum_{r=1}^{ns} X_r}{\sum X_r / \tau_{sr}}. \tag{11}$$

Table 1. Dissociation reactions with corresponding forward reaction rate constants.

	Reaction	Partner	$C_f\left(\frac{m^3}{mol \cdot s}\right)$	η	$\theta_d\,(K)$
1	$N_2 + M \rightleftharpoons N + N + M$	all molecular species	3.70×10^{15}	-1.6	113200
		all atomic species	1.11×10^{16}	-1.6	113200
2	$O_2 + M \rightleftharpoons O + O + M$	all molecular species	2.75×10^{13}	-1.0	59500
		all atomic species	8.25×10^{13}	-1.0	59500
3	$NO + M \rightleftharpoons N + O + M$	all molecular species	2.30×10^{11}	-0.5	75500
		all atomic species	4.60×10^{11}	-0.5	75500
4	$C_3 + M \rightleftharpoons C_2 + C + M$	all species	1.60×10^{10}	1.0	87480
5	$CO_2 + M \rightleftharpoons CO + O + M$	all species	1.20×10^{5}	0.5	36850
6	$C_2 + M \rightleftharpoons C + C + M$	all species	4.50×10^{12}	-1.0	70930
7	$CO + M \rightleftharpoons C + O + M$	all species	8.50×10^{13}	-1.0	129000
8	$CN + M \rightleftharpoons C + N + M$	all species	2.50×10^{8}	0.0	71000

* Reactions 1-3 from Park,[28] reactions 4-7 from Bhutta & Lewis[29] and reaction 8 from Park et al.[30]

Table 2. Exchange reactions with corresponding forward reaction rate constants.

	Reaction	$C_f\left(\frac{m^3}{mol \cdot s}\right)$	η	$\theta_d\,(K)$
9	$N_2 + O \rightleftharpoons NO + N$	3.18×10^{7}	0.10	37700
10	$NO + O \rightleftharpoons N + O_2$	2.16×10^{2}	1.29	19220
11	$CO + O \rightleftharpoons C + O_2$	2.00×10^{4}	1.00	69500
12	$CN + O \rightleftharpoons NO + C$	1.60×10^{7}	0.10	14600
13	$CO_2 + O \rightleftharpoons O_2 + CO$	3.00×10^{2}	1.00	18210
14	$CO + C \rightleftharpoons C_2 + O$	4.10×10^{4}	0.50	59790
15	$N_2 + C \rightleftharpoons CN + N$	2.00×10^{8}	0.00	23200
16	$CN + C \rightleftharpoons C_2 + N$	5.00×10^{7}	0.00	13000
17	$C_3 + C \rightleftharpoons C_2 + C_2$	1.70×10^{3}	1.50	19580
18	$CO + N \rightleftharpoons CN + O$	2.00×10^{8}	0.00	38600
19	$CO + N \rightleftharpoons NO + C$	9.00×10^{10}	-1.00	53200
20	$CO + CO \rightleftharpoons CO_2 + C$	1.00×10^{-3}	2.00	72390
21	$C_2 + CO \rightleftharpoons C_3 + O$	1.20×10^{7}	0.00	43240
22	$CO + CO \rightleftharpoons C_2 + O_2$	9.20×10^{5}	0.75	163300
23	$CO + NO \rightleftharpoons CO_2 + N$	1.00×10^{-3}	2.00	20980
24	$N_2 + O_2 \rightleftharpoons NO + NO$	6.69×10^{3}	-2.54	64639

* Reactions 9,10, and 24 are from Park,[28] reactions 12, 16, and 18 from Park et al.[30] and the remaining reactions are from Bhutta & Lewis.[29]

τ_{sr} is obtained from Millikan and White[32] using

$$\tau_{sr} = \frac{1}{p}\exp\left[A_{sr}\left(T^{-1/3} - 0.015\mu_{sr}^{1/4}\right) - 18.42\right],\ p \text{ in atm} \tag{12}$$

$$A_{sr} = 1.16 \times 10^{-3}\mu_{sr}^{1/2}\theta_{v,s}^{4/3} \tag{13}$$

$$\mu_{sr} = \frac{M_s M_r}{M_s + M_r} * 1000. \tag{14}$$

Here $\theta_{v,s}$ is the characteristic temperature corresponding to the energy level of the first excited vibrational mode. A factor of 1000 is used to compute μ_{sr} becuase the molecular weight used by Millikan and White was $kg/kmol$ and here the molecular weight is defined in kg/mol. τ_{cs} is from Park[25] to more accurately model the relaxation time in areas of high temperatures occuring just downstream of the bowschock.

$$\tau_{cs} = 1/C_s\sigma_v N_s \tag{15}$$

$$C_s = \sqrt{8RT/\pi M_s} \tag{16}$$

$$\sigma_v = 10^{21}\left(50000/T\right). \tag{17}$$

The viscosity of each species is computed using a Blottner curve fit shown in Eq. (18). The coefficients are obtained from Blottner,[33] Gupta,[34] and Candler[35] and are shown in Table 3. The mixture viscosity is then found using each species viscosity from a mixing rule obtained from Wilke.[36] This mixing rule is shown in Eqs. (19)–(21).

$$\mu_s = 0.1\exp\left[\left(A_s^\mu \ln\left(T\right) + B_s^\mu\right)\ln\left(T\right) + C_s^\mu\right] \tag{18}$$

$$\mu = \sum_{s=1}^{ns}\frac{X_s\mu_s}{\phi_s} \tag{19}$$

$$X_s = \frac{c_s}{M_s} \tag{20}$$

$$\phi_s = \frac{\sum_{r=1}^{ns} X_r\left[1 + \left(\frac{M_s}{M_r}\right)^{1/4}\right]^2}{\left[8\left(1 + \frac{M_s}{M_r}\right)\right]^{1/2}} \tag{21}$$

Table 3. Species viscosity coefficients.

species	A_s^μ	B_s^μ	C_s^μ
N_2	0.0268142	0.3177838	-11.3155513
O_2	0.0449290	-0.0826158	-9.2019475
NO	0.0436378	-0.0335511	-9.5767430
C_3	-0.0147000	0.8811000	-13.5051000
CO_2	-0.0195274	1.0478180	-14.3221200
C_2	-0.0031000	0.6920000	-12.6127000
CO	-0.0195274	1.0132950	-13.9787300
CN	-0.0025000	0.6810000	-12.4914000
N	0.0115572	0.6031679	-12.4327495
O	0.0203144	0.4294404	-11.6031403
C	-0.0001000	0.7928000	-13.4154000

The translation-rotation and vibration heat conductivities for each species are calculated from Eqs. (22) & (23). The total heat conductivities for each energy mode are combined similar to the viscosity using Eqs. (24) & (25). The diffusion velocity is calculated using Fick's law (Eq. (26)) and a constant Schmidt number (Eq. (27)) which yields acceptable results for species with similar molecular weights.

$$k_{T,s} = \mu_s \left(\frac{5}{2} c_{v,tr,s} + c_{v,rot,s} \right) \tag{22}$$

$$k_{V,s} = \mu_s \left(c_{v,vib,s} \right) \tag{23}$$

$$k_T = \sum_{s=1}^{ns} \frac{X_s k_{T,s}}{\phi_s} \tag{24}$$

$$k_V = \sum_{s=1}^{ns} \frac{X_s k_{V,s}}{\phi_s} \tag{25}$$

$$\rho_s v_{sj} = -\rho D_s \frac{\partial C_s}{\partial x_j} \tag{26}$$

$$Sc = \frac{\mu}{\rho D} = 0.5 \tag{27}$$

III. Surface Chemistry Model & Boundary Conditions

The surface chemistry model contains oxidation, recombination of atomic oxygen and sublimation of C, C_2 and C_3. The reactions and reaction probabilites for oxidation and recombination of atomic oxygen are obtained from Park.[10] The reaction probabilites for all three sublimation products were obtained experimentally by Palmer.[37] C_3 is included in most graphite ablation models because sublimation of graphite produces mostly C_3 with smaller amounts of C, C_2 and heavier carbon species.

Six surface reactions are taken into account. The first two reactions allow for surface removal of material through oxidation and the third equation gives the recombination of atomic oxygen. Nitridation is not included here but there has been recent experimetal work to determine the reaction probability by Suzuki and Fujita[38] as well as Park and Bogdanoff.[39] This reaction will be included in the future.

$$(C) + O_2 \rightarrow CO + O \tag{28}$$

$$(C) + O \rightarrow CO \tag{29}$$

$$(C) + O + O \rightarrow (C) + O_2 \tag{30}$$

The oxidation rates are based on kinetic theory giving

$$k_{w,r} = \alpha_r \sqrt{\frac{RT_w}{2\pi M_s}} \tag{31}$$

where α_r is the reaction probability for each reaction obtained experimentally to be

$$\alpha_1 = \frac{1.43 \times 10^{-3} + 0.01 \exp\left(-1450/T_w\right)}{1 + 2 \times 10^{-4} \exp\left(13000/T_w\right)} \tag{32}$$

$$\alpha_2 = 0.63 \exp\left(-1160/T_w\right) \tag{33}$$

$$\alpha_3 = 0.63 \exp\left(-1160/T_w\right). \tag{34}$$

There are three reactions for sublimation

$$(C) \rightarrow C \tag{35}$$

$$(C) \rightarrow C_2 \tag{36}$$

$$(C) \rightarrow C_3 \tag{37}$$

and for each reaction the mass flux is obtained from the Knudsen-Langmuir equation[40]

$$\dot{m}'_s = \alpha_s \left(p_{v,s} - p_s \right) \sqrt{\frac{M_s}{2\pi R T_w}} \tag{38}$$

where α_s is experimentally determined for each carbon species. The vapor pressure of the three carbon species is given by

$$p_{v,s} = \exp\left(\frac{P_s}{T_w} + Q_s \right) \quad p \text{ in } atm \tag{39}$$

Table 4. Sublimation reaction probabilities and vapor pressure coefficients.

	α_s	P_s	Q_s
C	0.14	-85715	18.69
C_2	0.26	-98363	22.20
C_3	0.03	-93227	23.93

* α_s from Palmer[37] and P_s and Q_s from.[26]

where Table 4 gives the reaction probabilities and vapor pressure coefficients for each sublimation reaction.

Boundary conditions are needed to couple the surface chemistry model with the gas model as well as set wall conditions for temperature and pressure. At the surface a surface energy balance needs to be solved to find temperature and a surface mass balance needs to be solved to find the mass fractions. A simplified surface energy balance is used to avoid a complicated flow/solid coupling and allowing the focus of the simulation to stay on boundary layer stability. The surface energy balance is

$$k_T \frac{\partial T}{\partial n} + k_V \frac{\partial T_V}{\partial n} + \sum_{s=1}^{ns} \rho h_s D_s \frac{\partial C_s}{\partial n} = \sigma \epsilon T_w^4 + \dot{m}'_w \sum_{s=1}^{ns} C_s h_{s,o} \tag{40}$$

where

$$h_{s,o} = \left(c_{v,s} + \frac{R}{M_s} \right) T + e_{v,s} + h_s^o + \frac{1}{2} \left(u_1^2 + u_2^2 + u_3^2 \right) \tag{41}$$

and all values and derivatives are taken at the wall. $\epsilon = 0.9$ for the carbon surface and σ is the Stefan-Boltzmann constant. Each derivative is taken normal to the surface where n represents the direction normal to the surface. 5^{th} order Lagrange polynomials are used to compute the normal derivatives at the surface. The surface mass balance for each species is

$$\rho_{s,w} v_w - \rho_w D_w \frac{\partial C_{s,w}}{\partial n} = \dot{m}'_s. \tag{42}$$

The total mass balance found from summing Eq. (42) is

$$\rho_w v_w = \dot{m}'_w \tag{43}$$

where the total mass flux is found from the sum of each species mass flux as

$$\dot{m}'_w = \sum_{s=1}^{ns} \dot{m}'_s. \tag{44}$$

For a wall with no velocity it is common to use pressure extrapolation or assume that $\frac{\partial p}{\partial n} = 0$ from the boundary layer assumptions. Here a finite wall velocity is obtained normal to the surface and the one-dimensional subsonic inlet conditions are used to set the wall pressure[41] for each case in Section IV. In Section V the pressure wall condition was to changed to 5^{th} order extrapolation using Lagrange polynomials.

IV. Validation

Three validation cases are computed with the shock-fitting code using the eleven species gas model and the surface chemistry model. Two cases are compared to Keenan's[2] computations and one case is compared to computations performed by Chen and Milos.[4] Recall that Keenan's work has served as a basis for the gas model and surface chemistry model. The notable difference between the two computations are that Keenan used a 2^{nd} order shock capturing method and computes a temperature profile within the ablator while here a 5^{th} order shock-fitting method suitable for direct numerical simulation of boundary layer instability is used.

A. Comparison to Keenan's $M_\infty = 15.99$ Computations of PANT Case 1

After implementing the gas model and surface chemistry model a code comparison was done to make sure that the models were implemented correctly. The first test case comes from Keenan's comparison to the Passive NoseTip Technology (PANT) experimental results.[42] The freestream conditions are given in Table 5. To be consistent with Keenan's naming this case is called PANT case 1. The geometry is a sphere cylinder with a nose radius of 0.635 cm. The grid is similar to Keenan's using 32 points on the surface and 91 points in the surface normal direction. In the shock-fitting code there is no computation of the temperature within the graphite ablative material but Keenan does compute the temperature within the ablator. For a better comparison, a curve fit of Keenan's computed results was used to set the surface temperatures rather than using the surface energy balance. Only the sphere region has been computed for comparison.

Table 5. Freestream conditions for PANT case 1.

M_∞	15.99
ρ_∞	$2.4093 \times 10^{-2}\ kg/m^3$
P_∞	$2026.0\ N/m^2$
C_{N_2}	0.7635
C_{O_2}	0.2365

Figure 1 gives a comparison of the stagnation line translation-rotation temperature and vibration temperature where $n = 0$ corresponds to the sphere stagnation point. In this and each following figure n represents the direction normal to the surface. In each figure the lines represent the shock-fitting computation and the symbols represent digitized data from Keenan's shock capturing computations. A large difference in the computed temperatures can be seen near the shock at approximately $n = 0.05\ cm$. This is due to the different computational methods used. The shock fitting method used in this paper uses Rankine-Hugoniot relations to compute the temperature behind the shock whereas shock capturing methods capture the shock and are commonly more diffusive. Similar results from Prakash et al.[17,43] also show a large difference in temperature behind a shock for thermochemical nonequilibrium flow between a shock fitting method and a shock capturing method. There is also a slight difference between the two temperatures near the stagnation point shown in Figure 1(b). This difference could be due to the different orders of the error for the different computational methods or the curve fit employed to set the wall temperature.

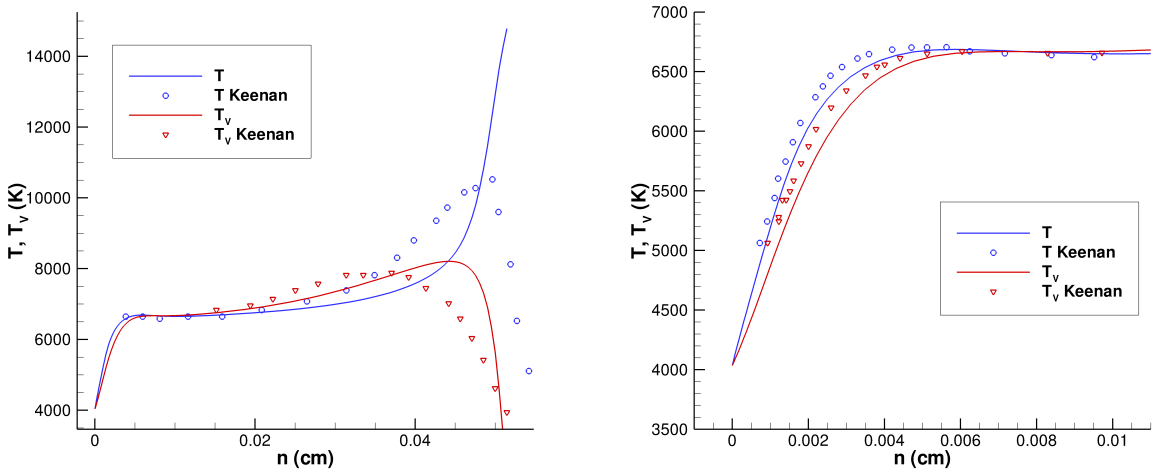

(a) (b)

Figure 1. Translation-rotation temperature and vibration temperature comparison on the stagnation line.

The shock standoff distance on the stagnation line for the shock fitting method is 0.0515 cm. It is difficult to tell exactly where the shock lies for the shock capturing method but qualitatively the shock location between the two methods on the stagnation line agrees well. There is a difference in the temperature equilibration location for the shock fitting method ($n \approx 0.045\ cm$) and the shock capturing method ($n \approx 0.035\ cm$). For the shock fitting method the distance between the shock and the equilibration point is less. For the shock fitting method there is a much larger difference between the translation-rotation temperature and the vibration temperature behind the shock. This makes the vibration temperature increase quicker than the shock capturing method thus moving the equilibration point nearer to the shock. Physically the shock thickness will be thin when the continuum approximation is valid as it is here. The equilibration point of the shock fitting method may be physically more accurate as the shock is approximated as a line for a 2D calculation and the shock capturing method smears the shock over multiple grid points. This means that for the shock fitting method the vibration temperature is exactly its freestream value after the shock becuase it has not had time to relax whereas for the shock capturing method the vibration temperature rises across the shock due to shock smearing.

Figure 2 gives a comparison of the stagnation line mass fractions and the mass fractions at the sphere cylinder juncture. For both subfigures the comparison between the mass fractions shows only small differences towards the surface ($n \approx 0$) where the computed temperatures between the two methods are similar. Near the shock the computed mass fraction for N_2 has only slight differences even though the temperatures are not the same. This is because the computed temperatures for both methods downstream of the equilibration point are not high enough for N_2 to begin dissociating. Near the shock there are differences in the mass fractions of O_2, O, and NO due to a higher temperature computed by the shock fitting method causing O_2 to dissociate and then react with N_2.

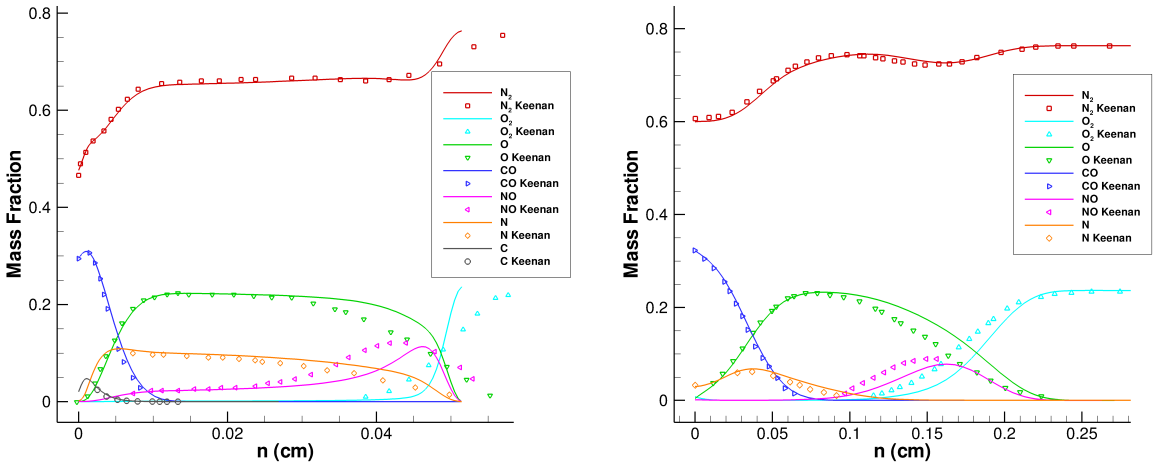

(a) (b)

Figure 2. Comparison of (a) mass fractions on the stagnation line, and (b) mass fractions at the sphere cylinder juncture to Keenan's computations.

A comparison of the surface chemistry model was obtained by comparing the total surface mass flux, $\dot{m}'_w$, and the surface mass fraction of each species shown in Figure 3. s is the surface streamline and is measured starting from the stagnation point. It should be noted that Keenan's data was digitized from a plot where the scale was small leading to the jumpiness in the data of Figure 3(a) which was not in the original plot. Good agreement is obtained for the surface mass flux. There is a 3% relative error at the stagnation point in surface mass flux and the profiles of the two computations are similar. s ≈ 1 corresponds to the sphere exit and at this point the mass flux is close to zero so for this case most of the ablation occurs near the nose. In Figure 3(b) the surface mass fractions are compated. The comparison between each species is good except there is some difference in CO_2. Recall from Section III that CO_2 is not produced at the surface so it must be formed in a gas phase reaction (reactions 5, 13, 20, and 23). The trend in CO_2 is similar and the difference between the two computations is small on the order of 10^{-4}.

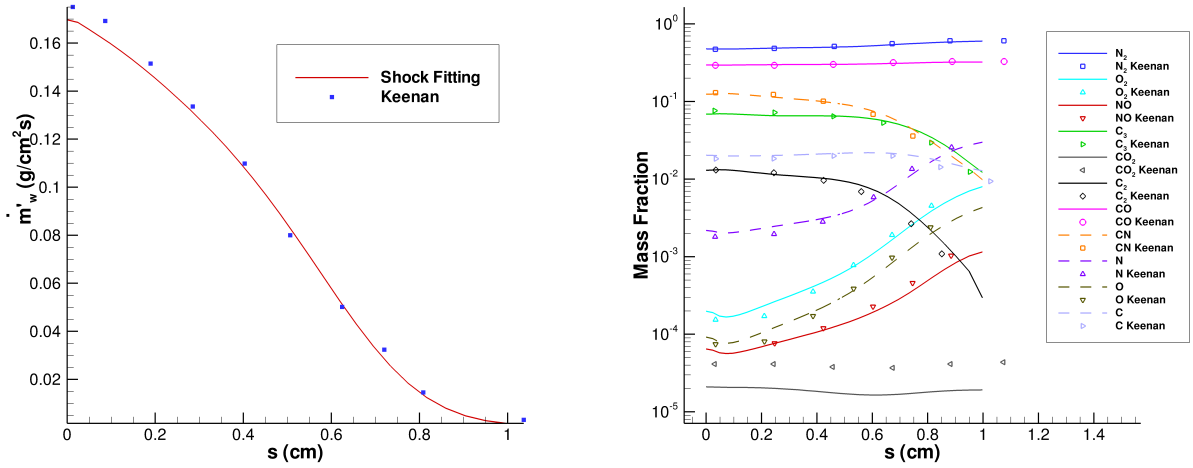

(a) Surface mass flux

(b) Surface mass fractions

Figure 3. Comparison of surface values to Keenan's computations where s is measured on the surface streamline and s = 0 corresponds to the stagnation point.

B. Comparison to Keenan's $M_\infty = 15.99$ Computations of PANT Case 2

A second PANT case was computed and compared with the computations of Keenan. Once again to be consistent with Keenan this case is called PANT case 2. The geometry and grid is the same as PANT case 1 and a curve fit to Keenan's surface temperature profile was used for better comparison. Only the nose region, i.e. the sphere, is computed for comparison. The grid is similar to Keenan's using 32 points on the surface and 91 points in the surface normal direction. The freestream conditions are given in Table 6.

Table 6. Freestream conditions for PANT case 2.

M_∞	15.99
ρ_∞	$2.4093 \times 10^{-1}\ kg/m^3$
P_∞	$20260.0\ N/m^2$
C_{N_2}	0.7635
C_{O_2}	0.2365

The mass fractions at the sphere exit plane are compared in Figure 4. Once again there is a good agreement near the wall and there is some error near the shock due to a higher computed translation-rotation temperature for the shock fitting method. In Figure 4(b) a close up of the mass fractions at the sphere exit is given. Similar to PANT case 1, there is good agreement in all the species except CO_2. The trends of CO_2 on the stagnation line are similar but the shock fitting value is slightly lower than Keenan's. Also, the value of CO_2 is quite small being on the order of 10^{-4} which is low enough to not effect the computational results for this case significantly. The reason for the difference may be numerical error.

Figure 5 compares the surface mass flux. s is the surface streamline and is measured from the stagnation point. At the stagnation point there is a 7% relative error between the two computations and the maximum relative error is 17% at $s = 0.142\ cm$. Keenan points out that the maximum mass flux should occur at the stagnation point so the increase in mass flux after the stagnation point is not physical. He also says that the modified Steger-Warming scheme that is used in the shock capturing method has some numerical issues near the stagnation point.

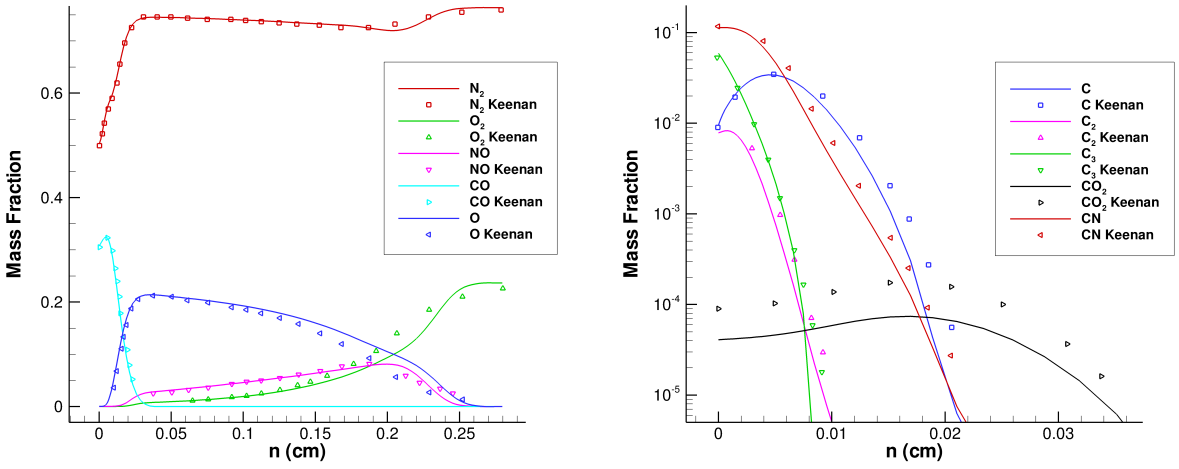

(a) (b)

Figure 4. Comparison of (a) mass fractions at the sphere exit and (b) a close up of the mass fractions at the sphere exit to Keenan's computations.

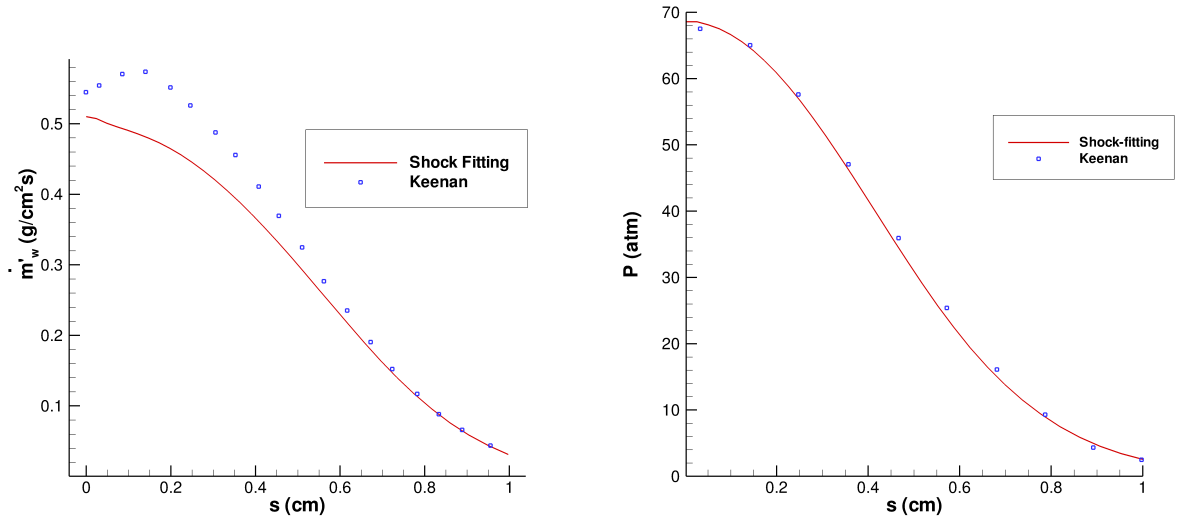

(a) Surface mass flux (b) Surface pressure

Figure 5. Comparison of surface values to Keenan's computations where s is measured on the surface streamline and s = 0 corresponds to the stagnation point.

C. Comparison to Chen and Milos' $M_\infty = 5.84$ Graphite Ablation Case

The gas model and surface chemistry model were compared to computations performed by Chen and Milos[4] of a sphere cone geometry with graphite ablation. This test case was chosen to compare with computations as well as an experiment performed at the Interactive Heating Facilities at NASA Ames Research Center. During this experiment a surface temperature was measured so instead of computing the surface temperature from a surface energy balance a curve fit to the experimental data is used. Chen and Milos use a different gas chemistry model than the shock-fitting method and test multiple surface chemistry models for intercomparison. None of the surface chemistry models they tested matched the model presented here so it was compared to their computations to find how it compared. The nose radius is $r = 1.905\ cm$ and the cone half angle is 10^o. The grid has 42 points on the surface and 101 points in the surface normal direction. The freestream conditions are given in Table 7.

Table 7. Freestream conditions for Chen and Milos' case.

M_∞	5.8434
ρ_∞	$3 \times 10^{-3}\ kg/m^3$
P_∞	$1671.36\ N/m^2$
C_{N_2}	0.6169
C_{NO}	0.0046
C_N	0.1212
C_O	0.2573

Figure 6 shows the comparison of the sphere surface mass blowing rates and the sphere surface pressure. The unfilled symbols represent digitized data from computations performed by Chen and Milos, the filled circles represent the experiment and the solid line represents current computations. Chen and Milos used four different types of surface chemistry models for one set of freestream conditions. Park (Nitridation) represents a surface chemistry model from Park[9,44,45] containing oxidation, nitridation and sublimation of C_3. Park (No Nitridation) represents the same model with the surface nitridation reaction turned off. A chemical equilibrium boundary condition represents that the gas phase and ablation boundary conditions are in equilibrium and the remaining surface chemistry model is a finite rate model proposed by Zhluktov and Abe[8] which includes oxidation, sublimation, and recombination but no nitridation. The ablation boundary conditions used in the shock fitting code represent the two experimental data points the best out of all the models. In Figure 6(a) near the stagnation point the current computations are almost identical to the experiment. This was not obtained by changing model parameters but rather the model just happens to represent this particular data set accurately which is encouraging.

The shock-fitting surface chemistry model is closest to the assumption of chemical equilibrium at the surface. The mass flux is less than the Park model with nitridation. The current surface chemistry model does not include nitridation but does include recombination of atomic oxygen and sublimation of C, and C_2 which is not included in Park with nitridation. Since sublimation of C and C_2 is small, the difference between the two models is mainly due to the added nitridation reaction as well as slight differences in the reaction probabilities. When the nitridation reaction is turned off the current surface chemistry model has a greater mass flux than Park. A comparison to the complex model of Zhluktov and Abe is not as straight forward. Zhluktov and Abe account for many more reactions and also account for active sites where chemical processes can take place. Near the stagnation point at the first available data point there is a 33% relative difference between Zhluktov and Abe and the current computations. The difference between the models decreases along the surface streamline but the relative difference is 81% at $s = 2.66\ cm$.

Figure 6(b) shows the sphere surface pressure profiles from the shock fitting method and Chen and Milos using the Park model with nitridation. The surface pressure boundary condition was not explicitly defined in Chen and Milos' paper while the pressure condition used in the shock-fitting code for this case is the 1D characterstic boundary condition for a subsonic inlet. The pressure obtained by the two methods shows a good agreement considering that the gas phase chemistry models are different as well as the surface chemistry model.

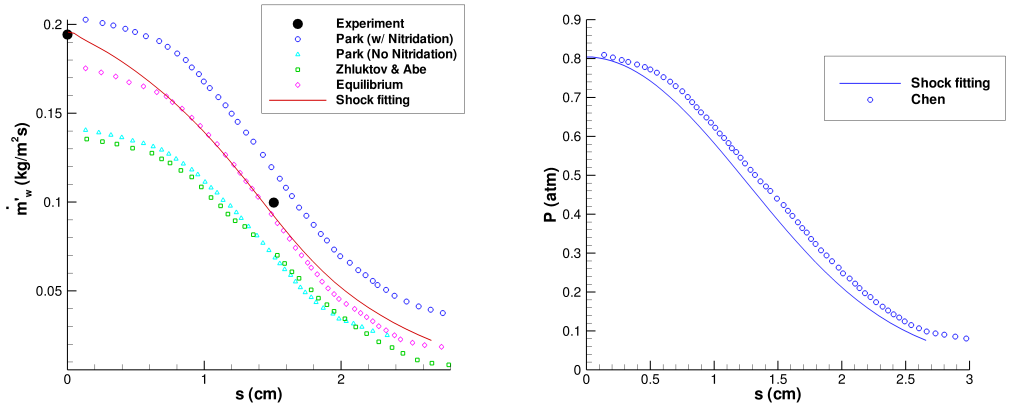

(a) (b)

Figure 6. Comparison of (a) sphere surface mass blowing rates and (b) sphere surface pressure to Chen and Milos' computations.

A comparison of the the species mass fraction along the stagnation line is given in Figure 7. The solid lines represent the shock-fitting code and the symbols represent Chen and Milos' computations with the Park nitridation surface chemistry model. There is a good comparison for the standard air species. Near the wall the mass fraction of O increases significantly for the shock-fitting method while it decreases for Chen and Milos. This is because the Park nitridation model does not include surface recombination of atomic oxygen while it is included in the shock-fitting surface chemistry model. The mass fraction for CN is higher at the wall for the Park nitridation model because nitridation is included while it is not in the shock-fitting model. There exists a significant difference in the mass fraction of C_3. In the shock-fitting code the mass fraction of C_3 decreases quickly along the stagnation streamline and reaches 10^{-5} at approximately 0.1 mm from the surface. For Chen and Milos C_3 decreases but not as quickly and reaches 10^{-5} at approximately 1 mm from the surface. While part of this may be attributable to diffusion—Chen and Milos use $Le = 1$ while shock-fitting uses $Sc = 0.5$—most would be attributed to differences in the gas model. Chen and Milos only inlcude dissociation of C_3 while the shock-fitting gas model includes dissociation of C_3 and two exchange rections (reactions 17 and 21) involving C_3.

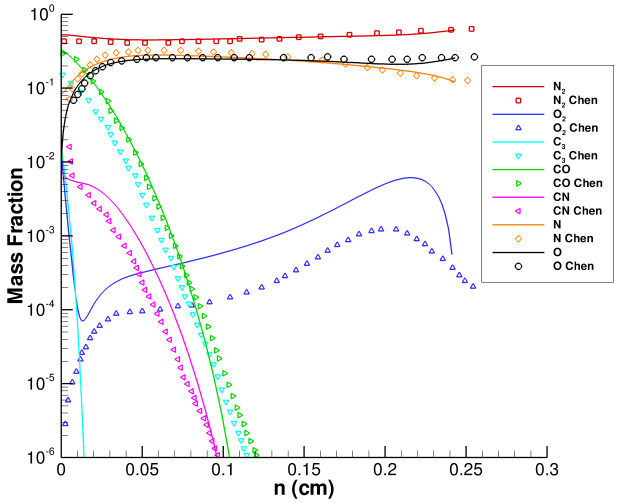

Figure 7. Comparison of species mass fraction along the stagnation line to Chen and Milos.

V. Hypersonic Boundary Layer Stability Results

A. Direct Numerical Simulation of $M_\infty = 15.99$ Blunt Cone

After validating the thermochemical nonequilibrium code a direct numerical simulation was performed to study hypersonic boundary layer stability with graphite ablation. The geometry is a sphere cone with a nose radius of 0.00635 m and a cone half angle of 7°. The freestream conditions are the same as PANT case 1 which are listed in Table 5. For this case $Re_u = 7.3 \times 10^6$ $/m$ and $h_{o,\infty} = 15.3$ MJ/kg. This is a high enthalpy case where thermochemical nonequilibrium affects should be significant and present well downstream of the nose. It should be noted that this case uses the surface energy balance (Eq. (40)) and surface pressure is extrapolated rather than using 1D characteristic conditions.

The computation of the sphere cone is performed in separate zones. The first zone encompasses the sphere region of the geometry and the following zones lie along the cone surface. Each zone is computed separately with boundary information being passed from the previous zone i.e. zone 2 is the first zone on the cone and it obtains boundary information on one boundary from zone 1. A grid convergence study was performed to verify that the grid in zone 1 was converged. The zone 1 grid is a body fitted, strutctured grid with 122 points in the streamwise direction and 121 points in the wall normal direction. Figure 8(a) compares the solution of P, T, and U_t for the 122 x 121 grid with a 242 x 241 grid at the sphere cone juncture. Here U_t is the velocity tangent to the sphere surface and each value has been nondimensionalized by its value at the shock represented by the subscript s. The difference between the two grids is minimal. Figure 8(b) shows the surface mass flux along the surface streamline starting at the stagnation point for the 242 x 241 grid and the 122 x 121 grid. The largest relative difference is 0.9% at the stagnation point. This slight difference is only in the first couple points near the stagnation line and could be due to the singularity in the grid metrics at this point. However, the difference is still small and the 122x121 grid was deemed converged.

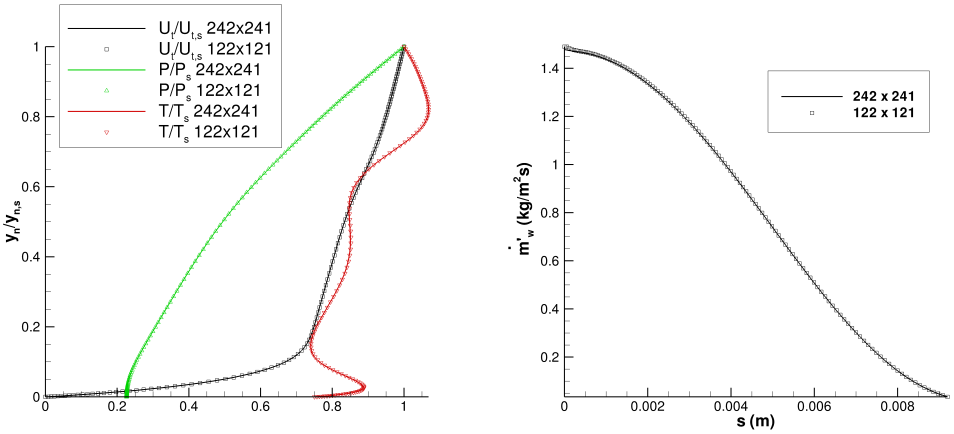

(a) Three profiles are shown: P, T, and U_t. Each is nondimensionalized by its value at the shock represented by the subscript s. Each profile is plotted normal to the surface at the sphere cone juncture.

(b) Comparison of the wall mass flux along s, the streamwise distance along the surface starting from the stagnation point.

Figure 8. Comparison of the 242x241 grid solution with the 122x121 grid solution.

Figure 9 is a contour plot of the translation-rotation temperature and the vibration temperature for the thermochemical nonequilibrium case. Zone 1 is shown in Figures 9(a) & 9(c) and both zones are combined in Figures 9(b) & 9(d). The translation-rotation temperature reaches its maximum value of $14,783$ K directly behind the normal shock at the stagnation line but then cools as the flow moves downstream. The vibration temperature reaches its maximum value of $8,198$ K at approximately $X = -0.68$ cm along the stagnation line. In zone 2 the vibration temperature is higher than the translation-rotation temperature in a region near the cone surface that runs parallel to the surface colored red. In this region the vibration temperature is relaxing towards the lower translation-rotation temperature.

Figure 14 is a contour plot of the mass fraction for each air species. The carbon species are not shown because they are only near the wall and cannot be seen well in a contour plot. The mass fraction of N_2 in

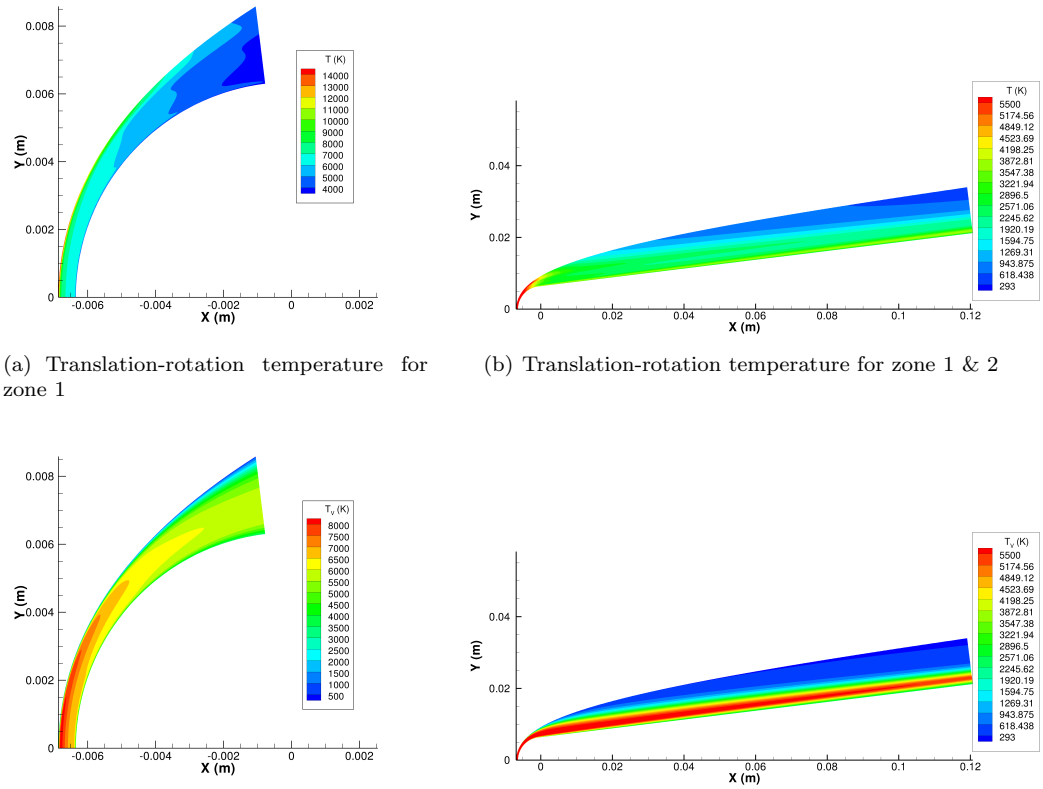

(a) Translation-rotation temperature for zone 1

(b) Translation-rotation temperature for zone 1 & 2

(c) Vibration temperature for zone 1

(d) Vibration temperature for zone 1 & 2

Figure 9. Contour plots of T and T_V. Thermal nonequilibrium is present throughout the length of the domain.

zone 2 is mostly its freestream value due to the two temperatures not being high enough for N_2 to dissociate. In the nose region O_2 is almost completely dissociated after the bow shock which increases the translation-rotation temperature. A significant mass fraction of O persists to the end of zone 2. O is recombining as it goes downstream due to the decrease in vibration temperature. $C_O \approx 0.18$ near the exit of zone 2 shows that chemical nonequilibrium is still present at the exit of zone 2.

To help understand the blowing caused by chemical reactions at the surface, Figure 10(a) shows the wall mass flux per area nondimensionalized by the freestream mass flux per area. This nondimensionalization is chosen because it is common in stability literature with wall blowing. The largest mass flux is at the stagnation point where the oxidation reactions as well as the sublimation reactions are all significant. The mass flux rapidly decreases along the surface streamline until it reaches $s/r \approx 1.55$ where it levels off and rises slightly before continuing to decrease all the way downstream. The rapid drop of wall mass flux corresponds to the rapid decrease in sublimation which is shown in Figure 11. The fact that there is still wall blowing in the cone region is due to the oxidation reactions.

Unlike many simulations of hypersonic boundary layer stability the wall temperature is not constant nor is the adiabatic condition ($\frac{\partial T}{\partial n} = 0$) enforced. Rather a surface energy balance (Eq. (40)) is solved which yields a temperature profile shown in Figure 10(b). Recall that the surface is assumed to be in thermal equilibrium so $T_V = T$ at the surface. The temperature has a maximum at the stagnation point and then drops rapidly as the flow expands. It is important to solve for the surface temperature in hypersonic flows with ablation as the wall temperature directly determines the reaction rate and probability for oxidation. It also plays a role in sublimation. In this case, as the wall temperature drops the wall mass flux drops as well.

To help understand the chemical processes at the surface Figure 11 shows the mass fraction for each species at the surface. The species with the largest mass fraction at the surface is N_2 but it does not react with the surface. The next largest mass fraction is CO. Recall from Eqns. (28) & (29) that the carbon surface can react with O and O_2 to form CO. These two reactions are the dominate reactions for the entire length

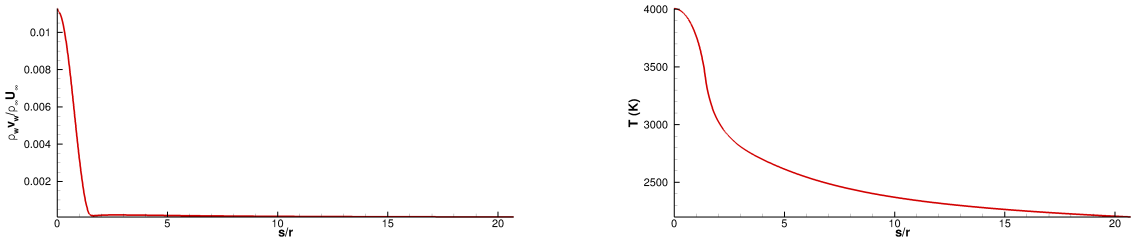

(a) (b)

Figure 10. Surface (a) nondimensional mass flux and (b) temperature. The surface is in thermal equilibrium.

of the surface i.e. they are responsible for the most mass loss due to ablation at the surface. Sublimation of C_3 (Eqn. (35)) is an order of magnitude less than CO at the stagnation point. In the sphere region it is the dominate form of sublimation until $s/r = 1.49$ which is slightly downstream of the sphere cone juncture at $s/r = 1.45$. For the cone region the dominate form of sublimation is sublimation of C. All three sublimation reactions drop of sharply after the sphere cone juncture due to a rapidly decreasing suface temperature and low surface pressure as the flow expands. There is a significant mass fraction of CN at the surface even though a nitridation reaction is not taken into account in the surface chemistry model. CN at the surface is due to reactions of ablation products with N_2 and NO. At the domain exit the only significant ablation product is CO which has a mass fraction of 0.24. At the exit of the domain the total mass flux is small so it is likely that the high mass fraction of CO comes from the ablation products reacting to form CO rather than O and O_2 reacting with the surface.

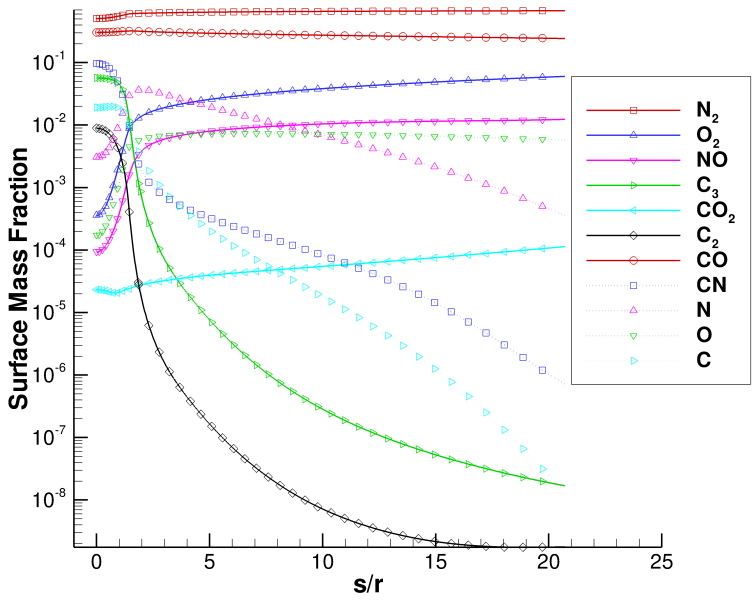

Figure 11. Surface mass fraction for each species.

Boundary layer profiles for the real gas case with ablation are given in Figure 15. Each profile is taken normal to the surface at a specific surface streamwise distance from the stagnation point. Figures 15(a)–15(f) show each of the eleven species. N_2 remains relatively constant across the boundary layer profiles as it only dissociates slightly after the bowshock and mainly reacts with the flow near the wall. O_2 increases near the wall for each profile due to surface recombination. There still exists a significant amount of atomic oxygen at

the farthest downstream station. In the nose region there are multiple carbon products with a mass fraction above 10^{-2}: C_3, CO, CN, C. After the nose region all of these species mass fraction at the wall decreases below 10^{-2} except CO which is the most significant carbon species downstream. At the wall in the farthest downstream station ($s/r = 20.0$) it has the highest mass fraction besides N_2 but it decreases quickly.

Figures 15(g)–15(l) show the boundary layer profiles of translation-rotation temperature and vibration temperature. On the stagnation line and at $s/r = 0.517$ the flow is near thermal equilibrium after the equilibration point. For the remaining streamwise stations there exists significant thermal nonequilibrium in the boundary layer which is helpful when evaluating the effects of thermal nonequilibrium on boundary layer stability i.e. this is a good test case to study thermal nonequilibrium effects.

The profiles of the velocity boundary layer are shown in Figures 15(g)–15(l). U_t is the velocity tangent to the surface and U_n is the velocity normal to the surface. Although it is unclear from the pictures there is a wall normal component at the surface i.e. $U_{n,w} \neq 0$. The scale of these pictures makes that fact unclear. In the nose region there is a large wall normal velocity away from the wall but as the flow progresses downstream the wall normal component moves to zero away from the surface and has a small non-zero component at the wall. The shape of the wall tangent velocity in the $s/r = 10.0$ and $s/r = 20.0$ profiles changes little.

1. *Ideal Gas Steady Solutions*

Three separate steady solutions were computed for stability simulations. The first is the full thermochemical nonequilibrium shock-fitting method with graphite ablation. The other two cases are ideal gas cases which use the same nonequilibrium code with the source terms turned off, the vibration energy held constant, and the mass fractions held to their freestream value. This is done so the viscosity, thermal conductivity, etc. are calculated the exact same way for the nonequilibirum and ideal gas cases. The first ideal gas case uses the temperature at the wall boundary from the thermochemical nonequilibrium graphite ablation case with the no slip boundary condition. The second ideal gas case matches the wall temperature as well as the wall mass flux of the thermochemical nonequilibrium graphite ablation case. This is done to test the effects of thermochemical nonequilibrium and wall mass flux on boundary layer stability. For ease of discussion the two ideal gas cases will be called ideal gas and ideal gas blowing while the full thermochemical nonequilibrium ablation case will be called real gas.

2. *Boundary Layer Stability*

After computing the steady solutions, freestream disturbances were imposed on the shock wave to find how the boundary layer behaved in the presence of graphite ablation and thermochemical nonequilibrium. The freestream disturbances imposed are weak planar fast acoustic waves in the freestream before reaching the shock at a zero incidence angle. The freestream variables can be written as the summation of the mean flow value and an oscillating component as

$$V_\infty = \begin{bmatrix} \rho_{1,\infty} \\ \vdots \\ \rho_{ns,\infty} \\ u_{1,\infty} \\ u_{2,\infty} \\ u_{3,\infty} \end{bmatrix} = \begin{bmatrix} \bar{\rho}_{1,\infty} \\ \vdots \\ \bar{\rho}_{ns,\infty} \\ \bar{u}_{1,\infty} \\ \bar{u}_{2,\infty} \\ \bar{u}_{3,\infty} \end{bmatrix} + \begin{bmatrix} \Delta\rho_{1,\infty} \\ \vdots \\ \Delta\rho_{ns,\infty} \\ \Delta u_{1,\infty} \\ \Delta u_{2,\infty} \\ \Delta u_{3,\infty} \end{bmatrix} \exp\left(i\left(k_x\left(x - \left(u_{1,\infty} + c_\infty\right)\right)t\right)\right) \tag{45}$$

where the disturbance amplitudes are defined by

$$\epsilon = \frac{\Delta P_\infty}{\gamma_\infty p_\infty} = \frac{\Delta\rho_\infty}{\rho_\infty} = \frac{\Delta u_{1,\infty}}{\gamma_\infty c_\infty}. \tag{46}$$

Here γ_∞ is the ratio of specific heats in the freestream and c_∞ is the speed of sound in the freestream. $\epsilon = 5 \times 10^{-4}$ and seven frequencies are imposed starting with a base frequency of 75 khz. Each frequency is a multiple of this base and the last frequncy is 525 khz. All frequencies are imposed simultaneously and their phases are set randomly.

For each of the three cases different unsteady wall boundary conditions were imposed. Each case uses pressure extrapolation to set the disturbance wall pressure. For the real gas case the surface mass balance

as well as the surface energy balance are used as boundary conditions. This means that the wall normal velocity will fluctuate as well as the wall temperature. For the ideal gas case the no slip condition is enforced on the disturbances and $\Delta T_w = 0$. For the ideal gas blowing case the mass flux is forced to remain constant and $\Delta T_w = 0$. When enforcing the mass flux to remain constant the wall normal velocity must fluctuate because density will fluctuate at the surface (recall Eq. (43)).

Figure 12 shows the disturbance amplitude of pressure at the wall nondimensionalized by the local meanflow pressure for three frequencies: 75 khz, 300 khz, and 525 khz. Each of the three meanflow cases is shown. For 525 khz the pressure amplitude is almost the same for all three cases. For 300 khz the pressure amplitude is larger for the real gas case than both ideal gas cases. This difference is most likely due to nonequilibrium effects and not surface mass flux as the two ideal gas cases are similar. For 75 khz all three cases have similar amplitudes for the pressure perturbation. All three frequencies for the ideal gas cases have similar pressure disturbance amplitudes. It could be that the wall mass flux is not large enough to significantly change the meanflow profiles between the two ideal gas simulations. In the future a three dimensional simulation will be run in the nose region. A lack of growth in pressure disturbances at the wall for all three cases indicates that the boundary layer is still stable.

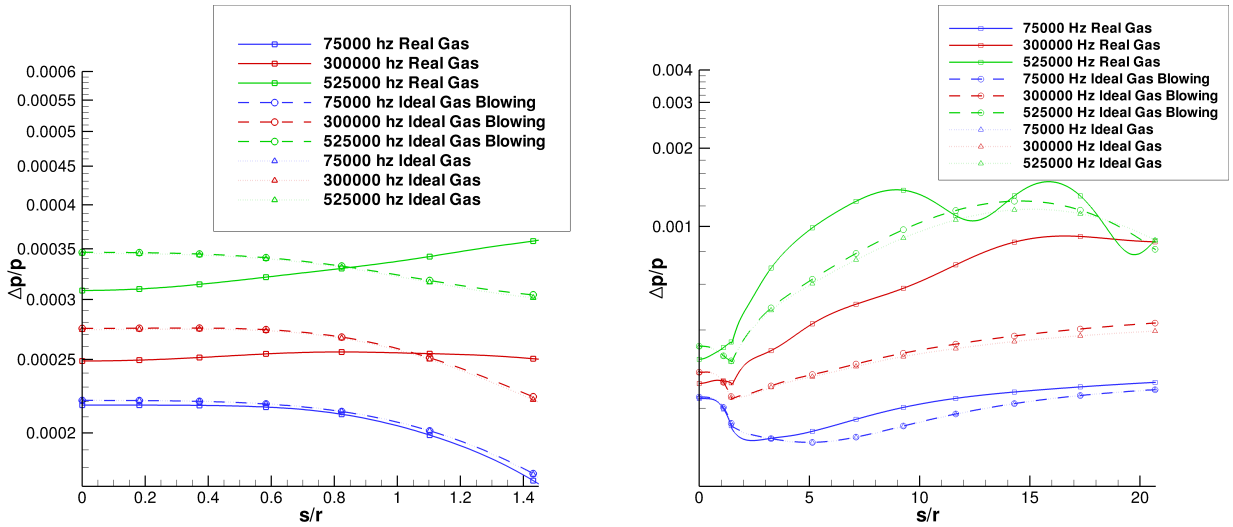

(a) (b)

Figure 12. Disturbance amplitude of pressure nondimensionalized by the local meanflow pressure in (a) zone 1 and (b) zone 1 and 2 at the surface. s is the surface streamline starting from the stagnation point.

For the real gas case and the ideal gas blowing case the wall normal velocity perturbation is non-zero and is shown in Figure 13. The wall normal velocity is nondimensionalized by the local velocity magnitude. Once again three frequencies are shown: 75 khz, 300 khz, and 525 khz. For the real gas case the amplitude of each frequency grows approximately three orders of magnitude along the surface of the sphere. At the sphere cone juncture the wall normal velocity magnitude for each frequncy decreases suddenly one order of magnitude and then remains relatively constant. For ideal gas blowing the disturbances grow two orders of magnitude along the sphere surface. Along the cone the 525 khz disturbance grows almost another order of magnitude but the other frequncies amplitude remains almost constant.

To give an idea of the disturbance amplitude of each species Figure 16 shows the species disturbance amplitude of select species nondimensionalized by the local meanflow density. The contour plots are only for 525 khz. N_2 is the most abundant species and has the largest disturbance amplitude of any species. The disturbance amplitude for N_2 is the largest near the surface of the cone. The disturbance amplitude of O_2 is largest behind the shock in the cone region. It is small near the wall because O_2 is mostly dissociated near the wall as shown in Figure 14(d). The disturbance amplitude for O is only large near the wall. It is the opposite of O becuase O_2 dissociates to from $2O$ so when there are large amounts of O_2 there are small amounts of O and vice versa. The maximum amplitudes of the O and O_2 disturbances are comparable at approximately 1×10^{-4}. The only significant gas phase species that contains carbon is CO. This species is entirely contained in the velocity boundary layer. Therefore the disturbance amplitude is only significant

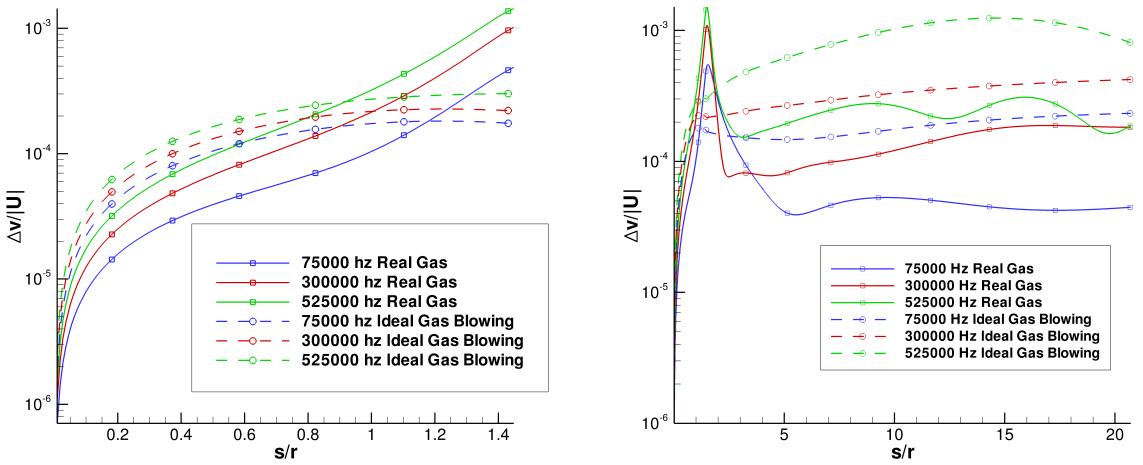

(a) (b)

Figure 13. Disturbance amplitude of wall normal velocity nondimensionalized by the local velocity magnitude in (a) zone 1 and (b) zone 1 & 2.

near the wall and in the boundary layer. The maximum amplitude of CO is near the wall and the amplitude decreases farther away from the wall.

Figure 17 shows the amplitudes of translation-rotation temperature and vibation temperature nondimensionalized by the local meanflow translation-rotation temperature for 525 khz. Figures 17(a) & 17(b) show the nose region while Figures 17(c) & 17(d) show the entire computational domain. In the nose region the vibration temperature amplitudes are the largest on the order of 10^{-2} while the translation-rotation temperature amplitudes are on the order of 10^{-4}. For both temperatures the amplitudes are strong directly behind the shock but the vibration temperature amplitude is also high near the surface in the stagnation region. It is interesting that the vibration temperature amplitude is high behind the shock because the vibration temperature is at its freestream value directly behind the shock before it starts to increase and equilibrate with the translation-rotation temperature (Figure 15(g)).

In the cone region of the geometry the vibration temperature perturbation amplitudes decrease gradually as the vibration temperature is relaxing. The amplitudes are the largest in the region where the vibration temperature is still relaxing towards the translation-rotation temperature. For the translation-rotation perturbation amplitudes in the cone region the largest amplitudes are at the surface and at the edge of the velocity boundary layer.

VI. Conclusion

A high-order shock-fitting method with thermochemcial nonequilibrium and graphite ablation has been presented. Research performed by Keenan and Candler has served as a basis for the gas phase modeling. An eleven species gas model without ionization is used for chemical nonequilibrium and the two temperature model is used for thermal nonequilibrium. Graphite ablation is simplified by neglecting surface recession, charring, pyrolysis, and ablation induced roughness. The surface reactions consist of oxidation, recombination of atomic oxygen and sublimation of C, C_2, and C_3.

Three cases were computed to validate the computational method. A comparison to Keenan's PANT 1 case shows that the shock-fitting method has a much higher temperature behind the shock on the stagnation line and the equilibration point is nearer the shock. The mass fraction of each species agrees well between the two cases except CO_2 where the difference is most likely due to numerical error. A comparison to Chen and Milos' computations shows that the surface mass flux of shock-fitting method lies between the Park with nitridation model and Zhluktov and Abe's model and is closest to an assumption of full equilibrium at the surface. Along the stagnation line C_3 decreases much quicker away from the wall for the shock-fitting

method than Chen and Milos' computations. This is most likely due to the different gas phase reactions between the two methods that contain C_3.

A direct numerical simulation was run for a 7° half angle blunt cone at Mach 15.99 to find how graphite ablation affects boundary layer stability. Three cases were run: real gas, ideal gas with blowing, and ideal gas. Both ideal gas cases set the surface temperature profile from the real gas simulation. For this case blowing was high in the nose and almost zero after the sphere cone juncture. Weak planar fast acoustic waves are used to perturb the steady base flow. A comparison of the pressure perturbation amplitude along the surface shows that the boundary layer is still stable for each case. The wall normal velocity perturbation amplitude increases three orders of magnitude for the real gas case and two orders of magnitude for the ideal gas blowing case. After the sphere cone juncture the wall normal velocity perturbations drop rapidly. In the nose region perturbation amplitudes for vibration temperature are almost two orders of magnitude larger than the translation-rotation perturbation amplitudes.

VII. Future Work

Future work includes updating the gas phase chemistry models with up to date forward reaction rates and equilibrium constants. The finite rate surface chemistry model from Zhluktov and Abe[8] will be added to test how different surface chemistry models affect boundary layer transition. Also, ionization energy will be included. A good representative geometry for re-entry vehicles with ablative heat shields is a sphere. In the future we would like to study how ablation affects boundary layer transition on a sphere and specifically the effects on three dimensional boundary layer instabilities.

Acknowledgements

The research was supported by the AFOSR/NASA National Center for Hypersonic Research in Laminar-Turbulent Transition. The computations are mainly run on XSEDE resources provided by TACC under grant number TG-ASC100002 supported in part by the National Science Foundation. The views and conclusions contained herein are those of the authors and should not be interpreted as necessarily representing the official policies or endorsements either expressed or implied, of the Air Force Office of Scientific Research or the U.S. Government.

References

[1]Ungar, E., "Ablation Thermal Protection Systems," *Science*, Vol. 158, No. 3802, 1967, pp. 740–744.

[2]Keenan, J., *Thermo-chemical Ablation of Heat Shields Under Earth Re-entry Conditions*, Ph.D. thesis, North Carolina State University, 1994.

[3]Zoby, E., Thompson, R., and Wurster, K., "Aeroheating Design Issues for Reusable Launch Vehicles – A Perspective," *AIAA 2004-2535*, 2004.

[4]Chen, Y. and Milos, F., "Navier-Stokes Solutions with Finite Rate Ablation for Planetary Mission Earth Reentries," *Journal of Spacecraft and Rockets*, Vol. 42, No. 6, 2005.

[5]Chen, Y. and Milos, F., "Three-Dimensional Ablation and Thermal Response Simulation Sys," *AIAA 2005-5064*, 2005.

[6]Lin, T., Sproul, L., and Olmos, M., "An Aerothermal Model for Ablating Heatshields," *AIAA 1994-247*, 1994.

[7]Potts, R., "Application of Integral Methods to Ablation Charring Erosion, A Review," *Journal of Spacecraft and Rockets*, Vol. 32, No. 2, 1995, pp. 200–209.

[8]Zhluktov, S. and Abe, T., "Viscous Shock-Layer Simulation of Airflow past Ablating Blunt Body with Carbon Surface," *Journal of Thermophysics and Heat Transfer*, Vol. 13, No. 1, 1999, pp. 50–59.

[9]Park, C., "Calculation of Stagnation-Point Heating Rates Associated with Stardust Vehicle," *AIAA 2005-190*, 2005.

[10]Park, C., "Effects of Atomic Oxygen on Graphite Ablation," *AIAA Journal*, Vol. 14, No. 11, 1976, pp. 1640–1642.

[11]Mack, L., "Boundary Layer Linear Stability Theory," AGARD report No. 709, 1984.

[12]Malik, M., "Numerical Methods for Hypersonic Boundary Layer Stability," *Journal of Computational Physics*, Vol. 86, No. 2, 1990, pp. 376–413.

[13]Stuckert, G. and Reed, H., "Linear Disturbances in Hypersonic, Chemically Reacting Shock Layers," *AIAA Journal*, Vol. 32, No. 7, 1994, pp. 1384–1393.

[14]Hudson, M., Chokani, N., and Candler, G., "Linear Stability of Hypersonic Flow in Thermochemical Nonequilibrium," *AIAA Journal*, Vol. 35, No. 6, 1997, pp. 958–964.

[15]Johnson, H., Seipp, T., and Candler, G., "Numerical Study of Hypersonic Reacting Boundary Layer Transition on Cones," *Physics of Fluids*, Vol. 10, No. 10, 1998, pp. 2676–2685.

[16]Ma, Y. and Zhong, X., "Receptivity to Freestream Disturbances of a Mach 10 Nonequilibrium Reacting Oxygen Flow over a Flat Plate," *AIAA 2004-0256*, 2004.

[17]Prakash, A., Parsons, N., Wang, X., and Zhong, X., "High-order Shock-fitting Methods for Direct Numerical Simulation of Hypersonic Flow with Chemical and Thermal Nonequilibrium," *Journal of Computational Physics*, Vol. 230, No. 23, 2011, pp. 8474–8507.

[18]Parsons, N., Zhong, X., Kim, J., and Eldredge, J., "High-order Shock-fitting Methods for Hypersonic Flow with Chemical and Thermal Nonequilibrium," *AIAA 2010-4997*, 2010.

[19]Johnson, H., Gronvall, J., and Candler, G., "Reacting Hypersonic Boundary Layer Stability with Blowing and Suction," *AIAA 2009-938*, 2009.

[20]Ghaffari, S., Marxen, O., Iaccarino, G., and Shaqfeh, E., "Numerical Simulations of Hypersonic Boundary-layer Instability with Wall Blowing," *AIAA 2010-706*, 2010.

[21]Li, F., Choudhari, M., Chang, C., and White, J., "Boundary Layer Transition over Blunt Hypersonic Vehicles Including Effects of Ablation-Induced Out-Gassing," *AIAA 2011-3303*, 2011.

[22]Keenan, J. and Candler, G., "Simulation of Ablation in Earth Atmospheric Entry," *AIAA 93-2789*, 1993.

[23]Keenan, J. and Candler, G., "Simulation of Graphite Sublimation and Oxidation under Re-Entry Conditions," *AIAA 94-2083*, 1994.

[24]Zhong, X., "High-Order Finite-Difference Schemes for Numerical Simulation of Hypersonic Boundary-Layer Transition," *Journal of Computational Physics*, Vol. 144, No. 2, 1998, pp. 662–709.

[25]Park, C., *Nonequilibrium Hypersonic Aerothermodynamics*, John Wiley & Sons Inc., New York, 1990.

[26]Dolton, T., Maurer, R., and Goldstein, H., "Thermodynamic Performance of Carbon in Hyperthermal Environments," *AIAA 68-754*, 1968.

[27]McBride, B., Heimel, S., Ehlers, J., and Gordon, S., "Thermodynamic Properties to 6000° for 210 Substances Involving the First 18 Elements," NASA SP-3001, NASA, 1963.

[28]Park, C., "On Convergence of Computation of Chemically Reacting Flows," *AIAA 85-0247*, 1985.

[29]Bhutta, B. and Lewis, C., "Low-to-High Altitude Predictions of Three-Dimensional Ablative Reentry Flowfields," *AIAA 92-0366*, 1992.

[30]Park, C., Howe, J., Jaffe, R., and Candler, G., "Chemical-Kinetic Problems of Future NASA Missions," *AIAA 91-0464*, 1991.

[31]Lee, J., "Basic Governing Equations for the Flight Regimes of Aeroassisted Orbital Transfer Vehicles," *Thermal Design of Aeroassisted Orbital Transfer Vehicles*, edited by H. F. Nelson, Vol. 96, AIAA, New York, 1985, pp. 3–53.

[32]Millikan, R. and White, D., "Systematics of Vibrational Relaxation," *Journal of Chemical Physics*, Vol. 39, No. 12, 1963, pp. 3209–3213.

[33]Blottner, F., Johnson, M., and Ellis, M., "Chemically Reacting Gas Viscous Flow Program for Multi-Component Gas Mixtures," SC-RR-70-754, Sandia National Laboratories, 1971.

[34]Gupta, R., Lee, K., and Sutton, K., "Viscous-Shock-Layer Solutions with Coupled Radiation and Ablation Injection for Earth Entry," *AIAA 90-1697*, 1990.

[35]Candler, G., "Computation of Thermo-Chemical Nonequilibrium Martian Atmospheric Entry Flow," *AIAA 90-1695*, 1990.

[36]Wilke, C., "A Viscosity Equation for Gas Mixtures," *The Journal of Chemical Physics*, Vol. 18, No. 4, 1950, pp. 517–519.

[37]Palmer, H. and Mordecai, S., *Chemistry and Physics of Carbon*, Marcel Dekker, Inc., NY, 1968.

[38]Suzuki, T. and Fujita, K., "Experimental Study of Graphite Ablation in Nitrogen Flow," *Journal of Thermophysics and Heat Transfer*, Vol. 22, No. 3, 2008, pp. 382–389.

[39]Park, C. and Bogdanoff, D., "Shock-Tube Measurements of Nitridation Coefficient of Solid Carbon," *Journal of Thermophysics and Heat Transfer*, Vol. 20, No. 3, 2006, pp. 487–492.

[40]Baker, R., "Graphite Sublimation Chemistry Nonequilibrium Effects," *AIAA Journal*, Vol. 15, No. 10, 1977, pp. 1391–1397.

[41]Hirsch, C., *Numerical Computation of Internal and External Flows, Volume 2: Computational Methods for Inviscid and Viscous Flows*, John Wiley & Sons, New York, 1990.

[42]Wool, M., "Final Summary Report Passive Nosetip Technology (PANT) Program," SAMSO-TR-75-250, SAMSO/RSSE, June 1975.

[43]Prakash, A., Parsons, N., Wang, X., and Zhong, X., "High-order Shock-fitting Methods for Hypersonic Flow with Chemical and Thermal Nonequilibrium," *AIAA 2010-4997*, 2010.

[44]Park, C., "Stagnation-Point Ablation of Carbonaceous Flat Disks, Park 1: Theory," *AIAA Journal*, Vol. 21, No. 11, 1983, pp. 1588–1594.

[45]Park, C., "Review of Chemical-Kinetic Problems of Future NASA Missions, 1: Earth Entries," *Journal of Thermophysics and Heat Transfer*, Vol. 7, No. 3, 1991, pp. 385–398.

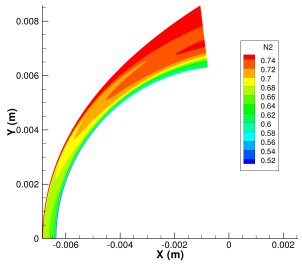

(a) N_2 mass fraction for zone 1

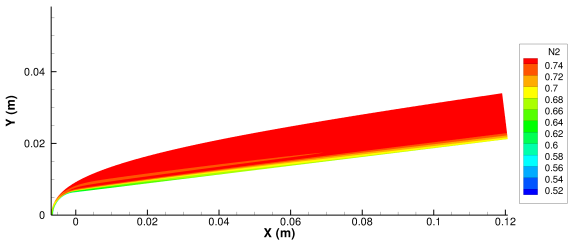

(b) N_2 mass fraction for zone 1 & 2

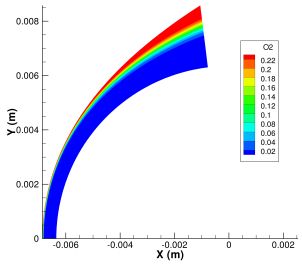

(c) O_2 mass fraction for zone 1

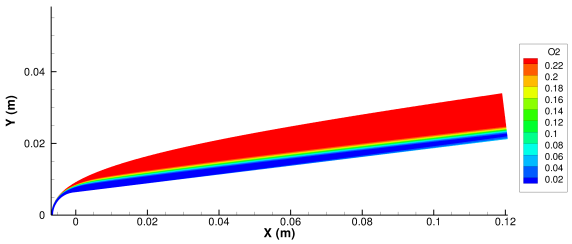

(d) O_2 mass fraction for zone 1 & 2

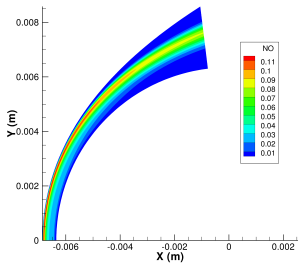

(e) NO mass fraction for zone 1

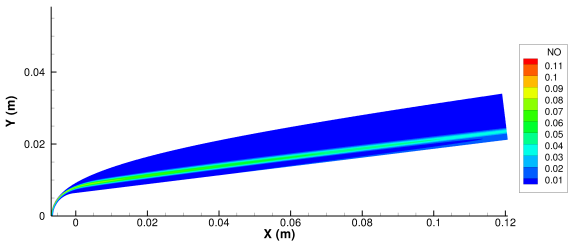

(f) NO mass fraction for zone 1 & 2

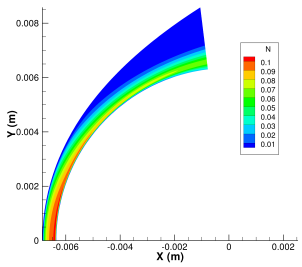

(g) N mass fraction for zone 1

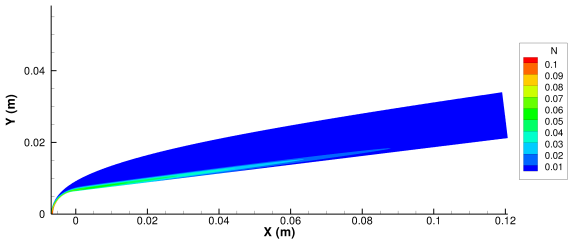

(h) N mass fraction for zone 1 & 2

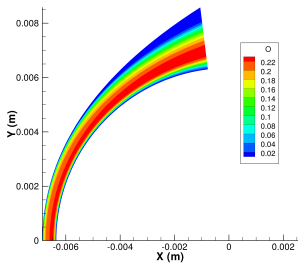

(i) O mass fraction for zone 1

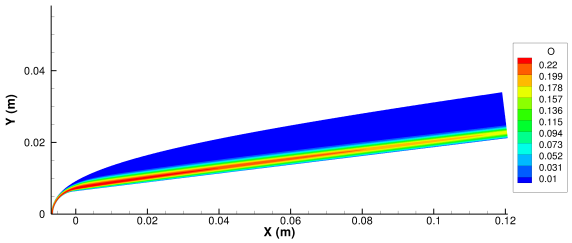

(j) O mass fraction for zone 1 & 2

Figure 14. Contour plots of mass fraction for each air species.

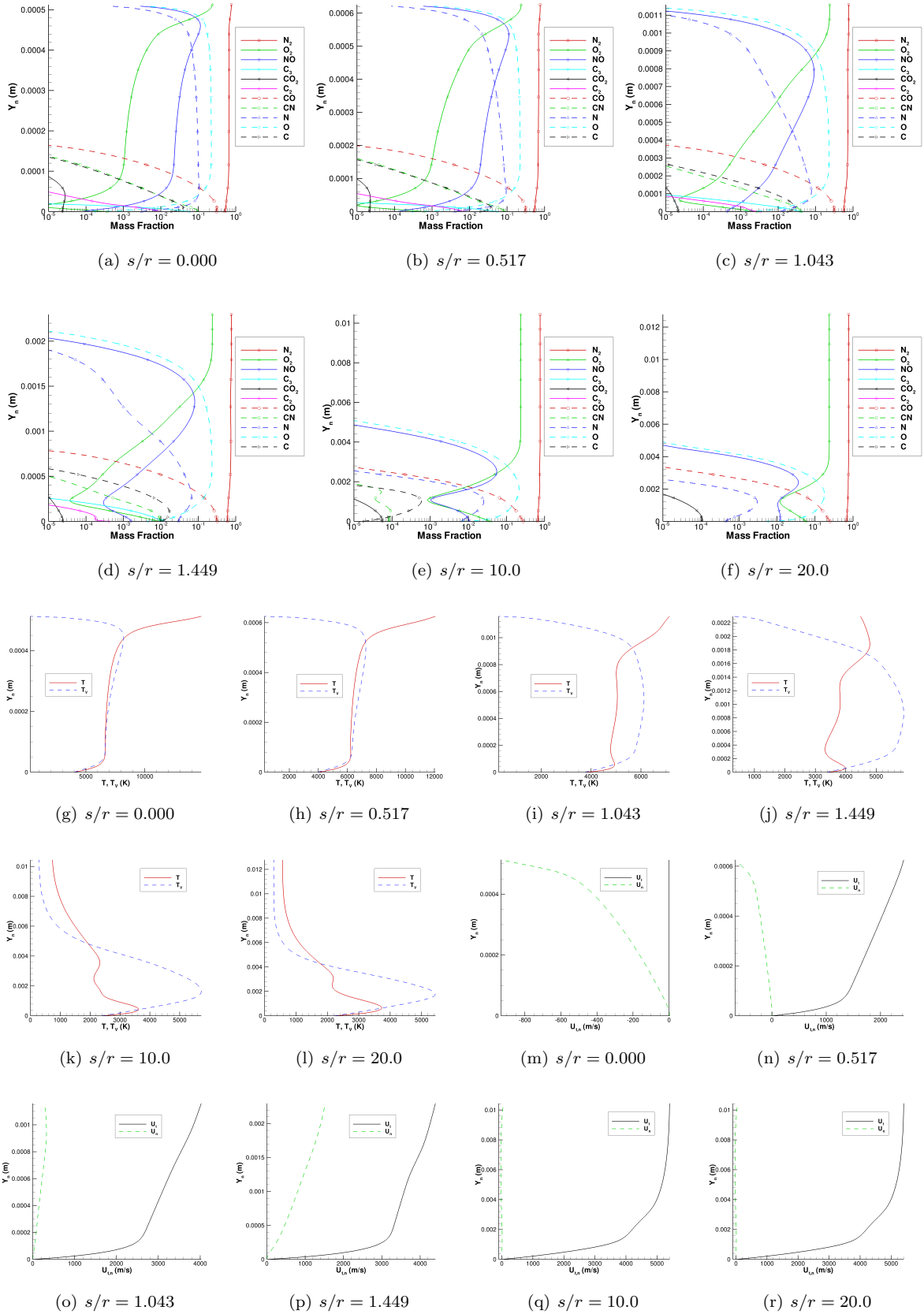

(a) $s/r = 0.000$ (b) $s/r = 0.517$ (c) $s/r = 1.043$

(d) $s/r = 1.449$ (e) $s/r = 10.0$ (f) $s/r = 20.0$

(g) $s/r = 0.000$ (h) $s/r = 0.517$ (i) $s/r = 1.043$ (j) $s/r = 1.449$

(k) $s/r = 10.0$ (l) $s/r = 20.0$ (m) $s/r = 0.000$ (n) $s/r = 0.517$

(o) $s/r = 1.043$ (p) $s/r = 1.449$ (q) $s/r = 10.0$ (r) $s/r = 20.0$

Figure 15. Profiles in the wall normal direction. s is the surface streamline measured from the stagnation point. s/r = 0 is the stagnation streamline and s/r = 1.449 is the sphere cone juncture.

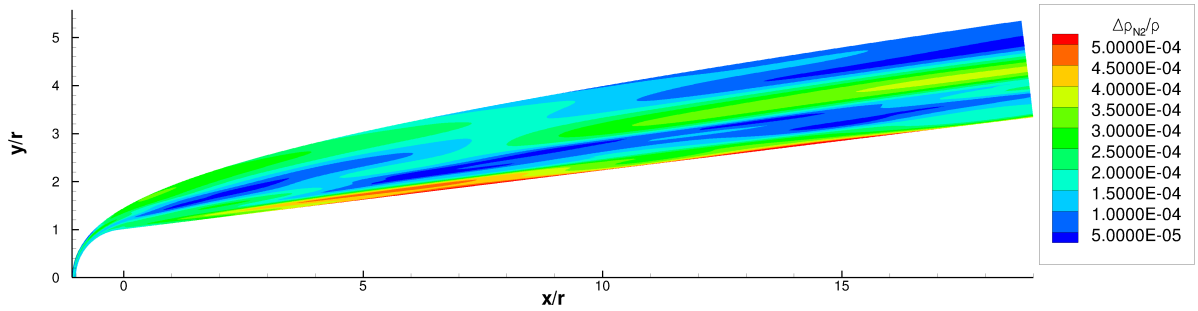

(a)

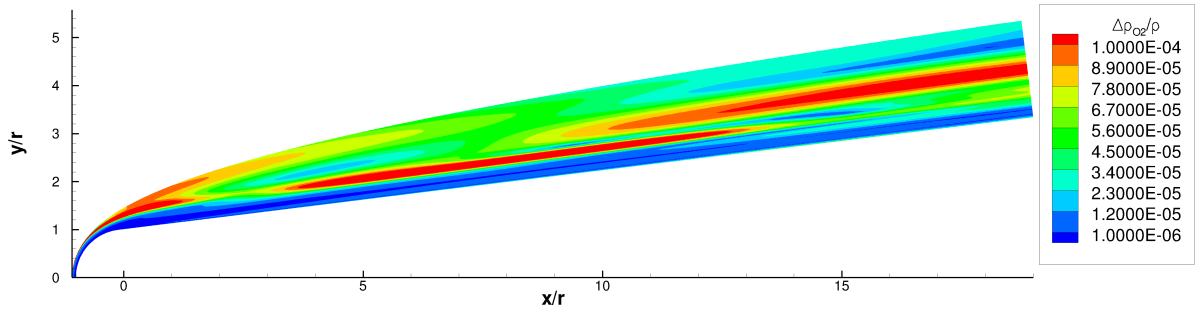

(b)

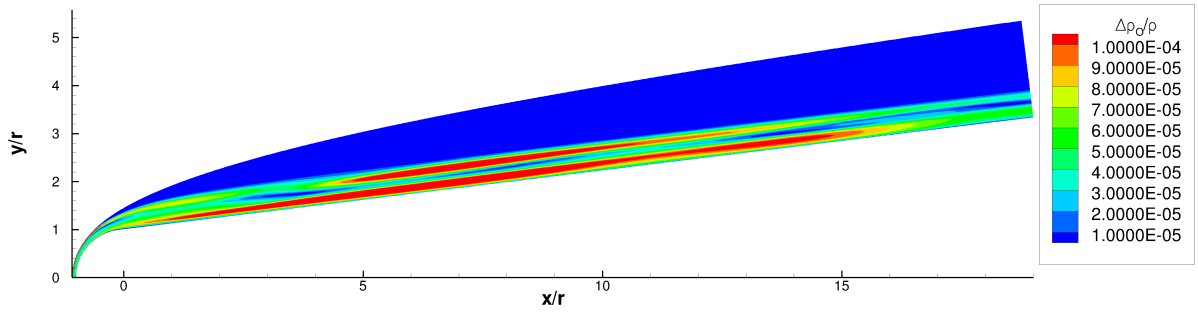

(c)

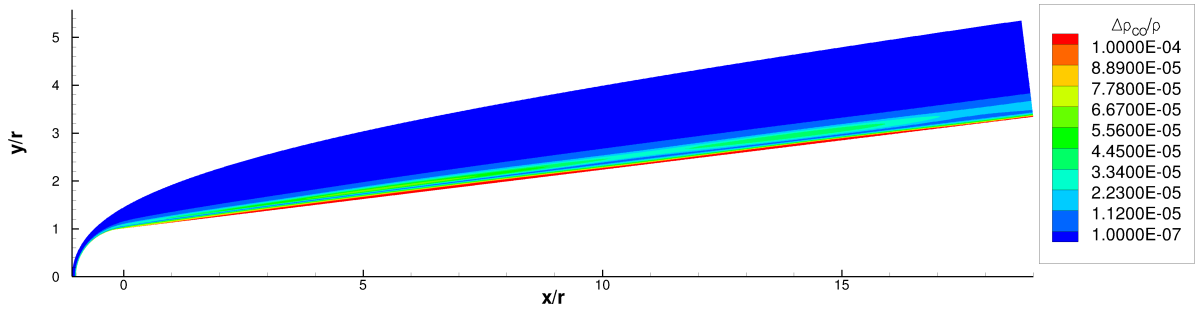

(d)

Figure 16. Disturbance amplitude for 525 khz of species density nondimensionalized by the local density for (a) N_2, (b) O_2, (c) O, and (d) CO.

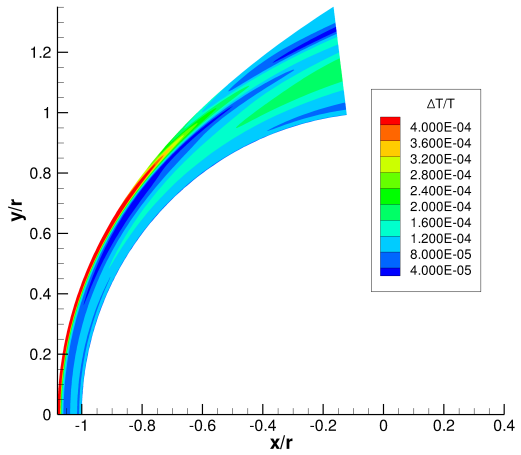

(a) translation-rotation temperature

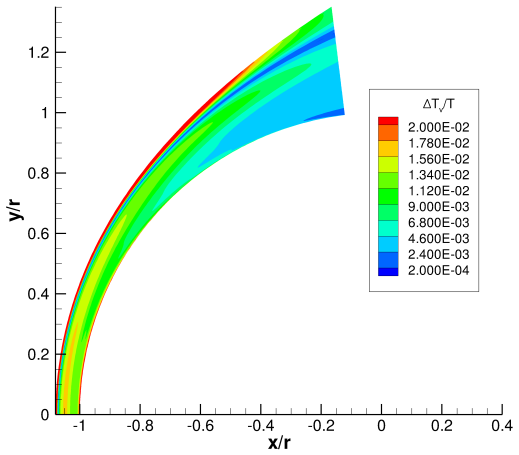

(b) vibration temperature

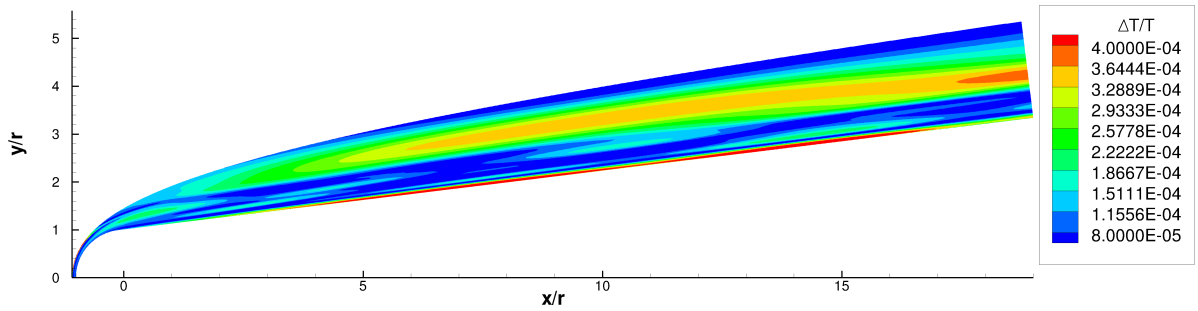

(c) translation-rotation temperature

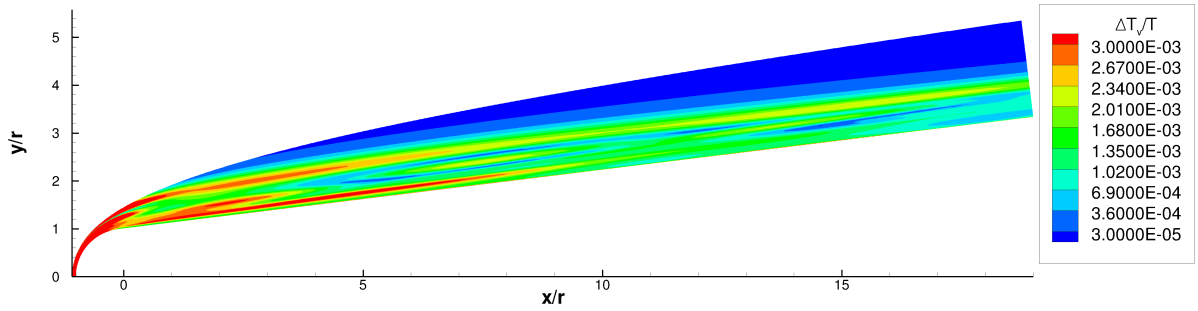

(d) vibration temperature

Figure 17. 525 khz disturbance amplitude of each temperature nondimensionalized by the local translation-rotation temperature.